NTNU
Norwegian University of
Science and Technology

Fabrication and Characterization of GaAs/AlGaAs Core-Shell Photonic Nanowires

Espen Rogstad

Master of Science in Electronics

Submission date:	November 2009
Supervisor:	Helge Weman, IET
Co-supervisor:	Dheeraj Dasa, IET

Norwegian University of Science and Technology
Department of Electronics and Telecommunications

Problem Description

This project deals with the fabrication and structural characterization of heterostructured GaAs nanowires with AlGaAs shells, grown by Au-catalyzed MBE. The nanowires will be grown on GaAs substrates with (111)B orientation, giving vertically standing nanowires. The grown nanowires will be structurally characterized with scanning electron microscopy (SEM) and optically characterized with low temperature µ-photoluminescence (PL). More specific the goals are:

1. To optimize the growth conditions of GaAs/AlGaAs core-shell heterostructure NWs. The main goal is to maximize the vapor-solid (VS) growth of AlGaAs in radial direction and minimize the vapor-liquid-solid (VLS) growth in axial direction. This can be achieved by experimenting with parameters such as substrate temperature, V/III ratio and the diameter of NWs. The structural characterization of these NWs will be done by SEM.

2. The effect of AlGaAs shell thickness and Al composition in the shell on the optical properties of NWs is to be determined by µ-PL.

Assignment given: 01. July 2009
Supervisor: Helge Weman, IET

Abstract

GaAs/AlGaAs core-shell nanowires (NWs) were grown on GaAs(111)B substrates by Au-assisted molecular beam epitaxy (MBE) to investigate how different Al compositions in the shell influences the structural and optical properties of the NWs. Investigations with a secondary electron microscope (SEM) revealed that an increase in Al content leads to an increase in radial growth rate and a decrease in the axial growth rate of the AlGaAs shell. Low temperature μ-photoluminescence (PL) measurements showed that there was great improvement in the luminescence for the GaAs/AlGaAs core-shell NWs compared to GaAs NWs without shell.

Preface

This Master thesis was undertaken at the Department of Electronics and Telecommunications at NTNU in Trondheim. It was a small part of a research group on semiconductor NWs led by Professor Helge Weman who also was the head supervisor for this project. Working on this thesis has given me a very valuable insight into first class scientific research on NW growth and characterization techniques along with hands-on experience with the equipment needed to fabricate and analyze nanosize structures. All the experimental work has been conducted at NTNU from January to March 2009. This thesis would not have been possible without the support of many people and I would like to thank all of them.

First and foremost, I would like to thank my supervisor Dheeraj Dasa for devoting numerous hours of lab work, for all the inspiring discussions, for replying to countless emails, for formulating a very interesting project task, for guidance throughout the process of writing this thesis, and the list goes on and on. It has been a pleasure working with him and I am greatly indebted for all the help he has put forth from start to finish of this project.

I want to thank Fervin Moses Anthonysamy for all the work and effort he has contributed, especially with everything related to PL measurements and PL data analysis. His advice and guidance has been crucial for the realisation of this thesis and I am truly grateful for that.

I want to thank Dr. Hailong Zhou for contributing to task organizing and formulation, for guidance on how to operate a SEM and for invaluable discussions. His enthusiasm and seemingly endless knowledge has been a true inspiration.

Many thanks goes to Associate Professor Antonius T. J. van Helvoort for TEM tutoring and analysis and to Dr. Thang Ba Hoang for his pivotal guidance in PL spectrum analysis.

I would also like to thank my head supervisor Professor Helge Weman and Professor Bjørn-Ove Fimland for all the assistance, organizing and feedback during this work.

Finally, special thanks go to my girlfriend Kristin for all her support and encouragement.

Thesis Outline

Chapter 1 gives an introduction to the work done in this project with some examples of possible applications for semiconductor NWs and a short description of how the NWs are fabricated. **Chapter 2** gives a theoretical insight in the physical properties of semiconductor crystal structures and how these can differ from bulk to the nanosize regime. This chapter also explains the basic concepts of NW growth by both VLS and VS mechanisms. **Chapter 3** describes the actual equipment used to first fabricate the NW samples and then characterizing them both structurally and optically. **Chapter 4** presents the results of the structural and optical characterization of the samples along with a discussion of the most important findings. Finally general conclusions are stated in **Chapter 5** along with a few suggestions for future work on NW heterostructures.

Contents

Nomenclature **viii**

1 Introduction **1**

2 Theory **3**

2.1 Crystal Structures . . . 3

2.1.1 Energy bands . . . 9

2.1.2 Surface states . . . 10

2.2 GaAs/AlGaAs core-shell heterostructures . . . 12

2.2.1 Band structure of GaAs/AlGaAs core-shell NWs . . . 14

2.3 Density Of States . . . 18

2.4 Growth mechanisms . . . 19

2.4.1 Vapor-Liquid-Solid (VLS) growth . . . 19

2.4.2 Vapor-Solid (VS) growth mechanism . . . 21

2.4.3 Diffusion induced growth model . . . 23

3 Materials and Methods **27**

3.1 Materials . . . 27

3.1.1 Molecular Beam Epitaxy (MBE) . . . 27

3.1.2 Secondary Electron Beam (SEM) 29
3.1.3 Transmission Electron Microscopy (TEM) 30
3.1.4 Photoluminescence (PL) 31
3.2 Methods 33
3.2.1 Growth Procedure 33
3.2.2 Structural characterization 34
3.2.3 Optical Characterization 35

4 Results and Discussion **37**
4.1 Structural Characterization 37
4.2 Optical Characterization 46

5 Conclusion **55**

References **63**

Nomenclature

bcc Body centred cubic

CB Conduction Band

CVD Chemical Vapor Deposition

DIGS Disorder-Induced Gap State

DOS Density Of States

eV Electron Volt

EWF Effective Work Function

fcc Face centred cubic

LEED Low Energy Electron Diffraction

LVFeSEM Low Voltage Field Emission SEM

MBE Molecular Beam Epitaxy

MIGS Metal-Induced Gap State

ML Monolayer

NW Nanowire

PL Photoluminescence

PT Polytypism

QD Quantum Dot

QW Quantum Well

QWR Quantum Wires

RHEED Reflection High Energy Electron Diffraction

sc Simple cubic

SEM Secondary Electron Microscope

STEM Scanning TEM

TEM Transmission Electron Microscope

UDM Unified Defect Model

VB Valence Band

VLS Vapor-Liquid-Solid

VP Variable Pressure

VS Vapor-Solid

WZ Wurtzite

ZB Zincblende

List of Figures

2.1 Illustration of scc, bcc and fcc lattices 4

2.2 Illustration of a hexagonal lattice 5

2.3 ZB and WZ crystal structures 5

2.4 ABAB and ABCABC stacking sequences 6

2.5 Stacking fault example 7

2.6 TEM of WZ GaAs NW with stacking faults 8

2.7 Typical dispersion relation 9

2.8 Surface states illustration 1 11

2.9 Surface states illustration 2 11

2.10 Lattice constants for some common semiconductors 13

2.11 Band structure of AlGaAs/GaAs/AlGaAs sandwich 14

2.12 Illustration of a raditive recombination in a type I-c bandstructure . 16

2.13 Illustration of some possible radiative recombination processes . . . 17

2.14 DOS for 3D, 2D, 1D and 0D semiconductor structures 18

2.15 Thin film of Au on GaAs(111)B substrate 19

2.16 Au-Ga liquid alloy droplets on top of a GaAs(111)B substrate . . . 20

2.17 Growth of GaAs NWs 21

2.18 GaAs and GaAs/AlGaAs core-shell NWs 22

2.19 Dubrovskii's growth model illustration 24

3.1 Schematic drawing of MBE growth chamber 27
3.2 Example of RHEED intensity oscillations 29
3.3 Schematic drawing of SEM mode of operation 29
3.4 Schematic drawing of TEM mode of operation 30
3.5 Schematic drawing of PL setup mode of operation 31
3.6 Example of structural characterization of NW 34
3.7 Example of 2D layer measurement 35

4.1 Cross-sectional images of GaAs/AlGaAs core-shell NWs 37
4.2 Close-up of the top region of NWs 39
4.3 Structural sketch of NWs from sample A and sample B 39
4.4 Tapering ratio 42
4.5 NW length Vs. base diameter 43
4.6 NW length Vs. centre diameter 44
4.7 NW length Vs. top diameter 44
4.8 Top view of sample A and sample B 45
4.9 PL intensity Vs. energy and energy Vs. power sample A 47
4.10 PL intensity Vs. energy and energy Vs. power sample B 51

Chapter 1

Introduction

Semiconductor NWs have recently been devoted much attention because of their potential application in nanoscale electronic and photonic devices. Key characteristics of NWs are excellent mechanical strength, high-thermal conductivity, their ability to function as single electron transistors and single quantum dots [1].

This work focused on GaAs/AlGaAs core-shell NWs grown on GaAs(111)B substrates by MBE. NWs with the core-shell structural design can be used to realize laser diodes [2], light emitting diodes [3], field-effect transistors [4]-[5], solar cells [6] and sensors [7]. The bandgap difference between the AlGaAs shell and GaAs core (up to 0.74 eV higher for AlAs) prevents carriers to reach non-radiative states on the NW surface and significantly improves the efficiency of radiative recombination in the GaAs core. In addition to the improved radiative qualities the core-shell has a low lattice mismatch (~0.12%) which makes this structure an attractive one for making nearly strain-free axial and radial heterostructured NWs. While the GaAs core grows mainly in the axial direction by precipitation of solid GaAs underneath a Au-Ga alloy droplet in a Vapor-Liquid-Solid (VLS) growth mode, the AlGaAs shell grows both in the radial direction, by nucleation at the NW sidewalls (Vapor-Solid (VS) growth), and in the axial direction (VLS growth). This can be attributed to the shorter diffusion length of Al adatoms compared to Ga. The main goal of this work was to maximize the VS growth of AlGaAs in radial direction and minimize the VLS growth in axial direction. This can be achieved by increasing the Al content in the shell, lowering the growth temperature or increasing the V/III flux ratio. The structural characterization of the NWs grown was done with SEM. The second goal was to investigate how the AlGaAs shell thickness and Al composition in the shell influenced the optical properties of the NWs by using low temperature μ-PL. Finally a comparison between the optical response from GaAs and GaAs/AlGaAs core shell NWs was made to see if there was any improvement in surface state repression with AlGaAs shell.

Fabrication of NWs today is mostly done by two ways, by chemical vapor deposition (CVD) and MBE with CVD being the far most common. MBE is a method based predominantly on diffusion-induced mechanism, meaning that the dominant factor for NW growth comes from atoms landing on either the sidewalls or the substrate and then diffuses to the liquid alloy drop. The growth conditions of MBE allow detailed studies on the growth process suitable for theoretical modelling since no precursor decomposition mechanisms are required. MBE gives a larger length and aspect ratio at a lower material consumption compared to the CVD. NWs grown with MBE are typically 10-100 nm thick and have lengths up to several micrometers. MBE allows for very abrupt heterojunctions because of the very low growth rate and is therefore ideal for fabricating heterostructured NWs with sharp material interfaces in both axial and radial directions.

Chapter 2

Theory

2.1 Crystal Structures

A crystal is a solid in which identical groups of atoms are arranged in an orderly and periodic pattern. A group is known as a *basis* and it can consist of one or more atoms. Every basis is attached to a lattice point in what is known as the crystals *Bravais lattice*. The crystal is essentially build up of many identical parallelepiped *unit cells*, defined in three dimensions by the translation vectors $\mathbf{a}_1$, $\mathbf{a}_2$ and $\mathbf{a}_3$, such that the arrangement of atoms in the crystal looks the same when viewed from the point $\mathbf{r}$ as when viewed from every point $\mathbf{r}$´ translated by an integral multiple of the $\mathbf{a}$'s [8]:

$$\mathbf{r}' = \mathbf{r} + u_1\mathbf{a}_1 + u_2\mathbf{a}_2 + u_3\mathbf{a}_3 \tag{2.1}$$

Where u_1, u_2 and u_3 are arbitrary integers. There are 14 different Bravais lattices in three dimensions which in turn are divided into seven crystal systems; triclinic, monoclinic, orthorhombic, tetragonal, cubic, rhombohedral and hexagonal. One of the most common crystal systems in semiconductors is the cubic system, which consists of the simple-, body-centred- and face-centred-cubic lattices, illustrated in Figure 2.1.

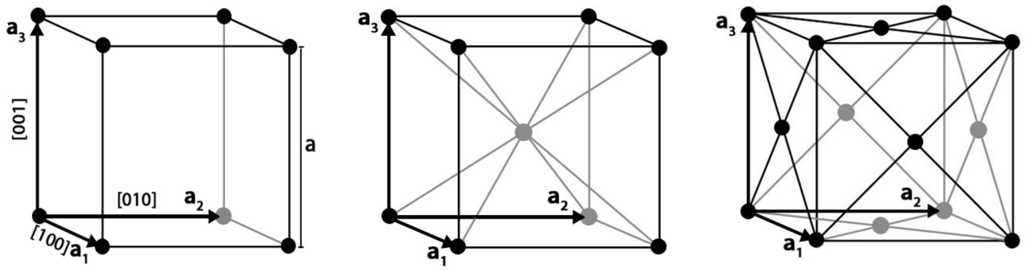

(a) Simple cubic (sc) (b) Body centred cubic (bcc) (c) Face centred cubic (fcc)

Figure 2.1: Illustration of scc, bcc and fcc lattices.

Directions and planes in crystals are described by a special notation system called *Miller indices.* A lattice defined by $\mathbf{a}_1$, $\mathbf{a}_2$ and $\mathbf{a}_3$ with vector direction $\mathbf{r}$ = h$\mathbf{a}_1$ + k$\mathbf{a}_2$ + l$\mathbf{a}_3$, is described as [*hkl*] where *h*, *k* and *l* are the lowest reduced integers. The notation <*hkl*> denotes all directions that are equivalent to [*hkl*] by symmetry. Lattice planes in the crystal are written (*hkl*) and are defined as the smallest integers, *h*, *k* and *l*, proportional to the reciprocal of the intercepts of the plane with the three crystal axes of unit length. The notation {*hkl*} denotes all planes that are equivalent to (*hkl*) by symmetry of the lattice. For all the notations a negative integer is denoted with a bar $\bar{\mathrm{h}}$ instead of -h. In cubic crystals, the direction [*hkl*] is perpendicular to the plane (*hkl*) having the same indices, but this is not generally true in other crystal systems.

For hexagonal structures it is often common to use a modified version of the Miller indices called the *Miller-Bravais indices*, with four indices (*hkil*) instead of three. The hexagonal system consists of three "**a**" axes, with 120° angles between each other, perpendicular to a "**c**" axis as indicated in Figure 2.2. It is important to note that only three indices are needed to identify planes and directions since the sum of the reciprocal intercepts with $\mathbf{a}_1$, $\mathbf{a}_2$ and $\mathbf{a}_3$ equals zero, i.e. *h* + k + *i* = 0.

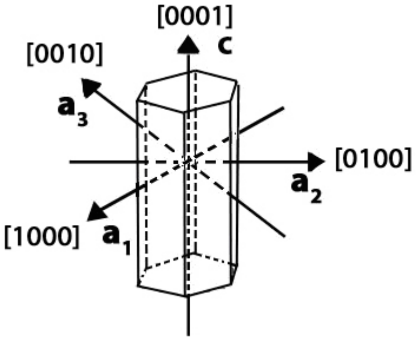

Figure 2.2: Illustration of a hexagonal lattice with the vectors $\mathbf{a}_1$, $\mathbf{a}_2$, $\mathbf{a}_3$ and $\mathbf{c}$ depicted.

The most common crystal structure for bulk III-V semiconductors is *zincblende* (ZB) which basically consists of two fcc lattices with bases at the coordinates 000 and $\frac{1}{4}\frac{1}{4}\frac{1}{4}$ illustrated in Figure 2.3a. III-V semiconductor NWs however often adopt the hexagonal *wurtzite* (WZ) phase or rotational twin layers resulting in polytypism (PT) between WZ and ZB structures. The transition from ZB in bulk to WZ in NWs is common in many III-V semiconductor compounds, like GaAs, AlGaAs and GaP to mention a few ([9], [10], [11], [12], [13], [14]). An illustration of a hexagonal WZ structure is shown in Figure 2.3b.

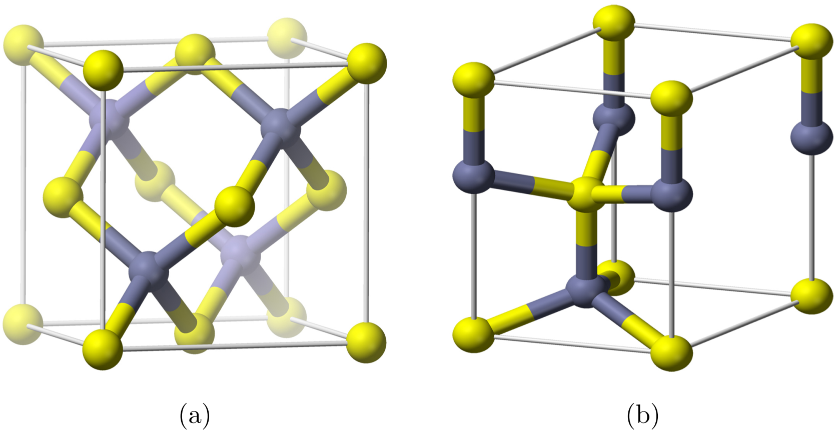
(a) (b)

Figure 2.3: Crystal structures : (a) Conventional unit cell of a ZB strucure; (b) Conventional unit cell of a WZ structure. For GaAs the yellow spheres represents Ga atoms and the purple spheres represents As atoms.

The NWs can alternate between ZB and WZ phases many times during the length of the wires with varying length of ZB and WZ segments. A shift between the two structures is known as a *stacking fault* and its one of the challenges facing NW fabrication today. The ZB and WZ structures are identical except that WZ has an ABAB stacking sequence along the [111] direction while ZB has ABCABC along [0001], see Figure 2.4, each letter representing a bilayer.

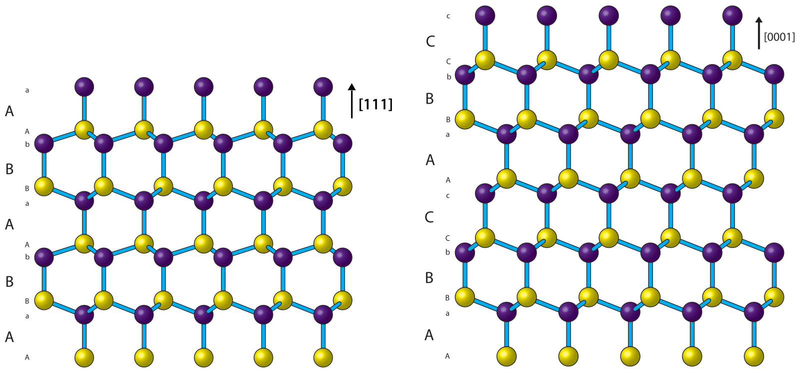

(a) (b) .

Figure 2.4: Stacking sequences: (a) ABAB stacking along the [111] direction for the WZ structure; (b) ABCABC stacking along the [0001] direction for the ZB structure.

This seemingly small difference leads to a band energy offset of several tens of milli-electronVolts (meV) which alter the optical and charge-carrier transport properties of the NWs and leads to electron scattering at the interface between the two phases [15] [16]. A stacking fault in a WZ phase can be caused by the misplacement of just a single bilayer, the sequence ABABCBCB gives rise to a single ZB segment (ABC) in the WZ structure, see Figure 2.5a. On the other hand a ZB phase with a single bilayer misplaced, for instance ABCACBA, does not produce a WZ segment and is thus not a stacking fault. This abbreviation from the normal stacking order is called a *twin plane* and is defined as a mirror plane between two segments rotated by 60° from each other. At least two consecutive twin planes are required for a WZ segment to be created in a ZB structure, giving the sequence ABCACAC illustrated in Figure 2.5b.

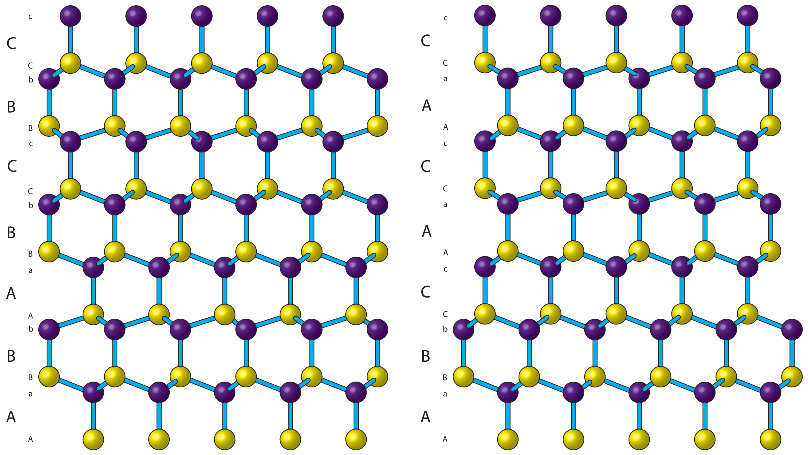

(a) (b)

Figure 2.5: (a) Stacking fault in a WZ structure with a misplacement of only one bilayer. The stacking sequence is here ABABCBCB which gives a single layer of ZB (ABC stacking) in the WZ structure. (b) Stacking fault in a ZB structure with two consecutive twin planes. The stacking sequence is here ABCACAC which gives a single WZ layer in the ZB structure.

The WZ phase often dominates for NWs with smaller diameter and/or grown at lower temperature than ZB dominated NWs. {1100} WZ planes might have a lower surface energy than {110} and {111}A/B ZB planes and this could explain why thinner NWs have a tendency to have WZ phase, but the exact process is quite complex and not yet fully understood. If the process of creating twin planes and PT could be properly controlled it could be used to produce superlattices from a single material and thereby removing the problems involved with lattice mismatch. In [17] [18] they showed that twin plane superlattices in theory could give rise to effects such as mini-band formation and zero energy gaps at the superlattice Brillouin zone boundary. Figure 2.6 shows a transmission electron microscopy (TEM) image of a semiconductor NW with a WZ structure but with a number of stacking faults resulting in short ZB segments.

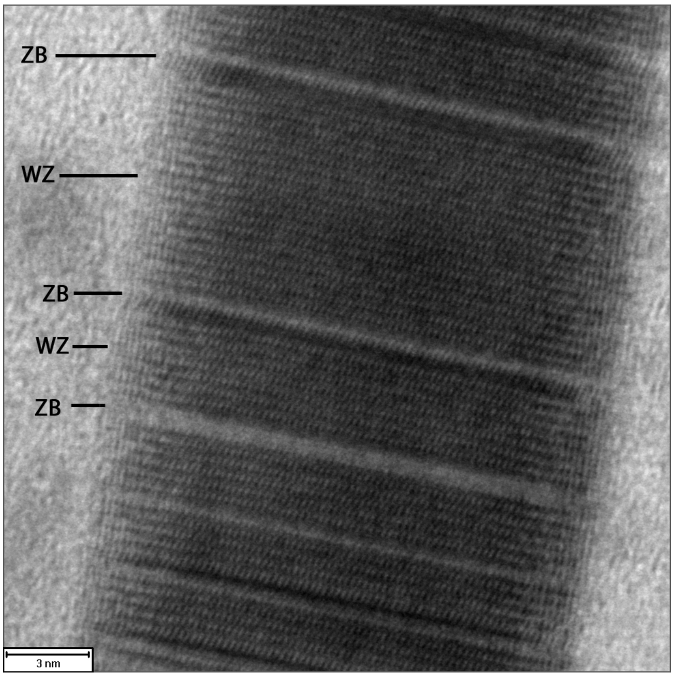

Figure 2.6: TEM image of a NW with WZ structure but with a number of stacking faults indicated as 'ZB' in the figure.

2.1.1 Energy bands

In crystals the electrons are arranged in *energy bands* separated by regions in energy for which no wavelike electron orbitals exist. Such forbidden regions are called *energy gaps* or *band gaps*, and result from the interaction of the conduction electron waves with the ion cores of the crystal. For semiconductors at zero temperature the energy bands below the band gap are filled while the bands above the band gap are empty. Most semiconductors have a band gap of around 1 eV. The energetically highest occupied energy band is called the valence band (VB) and the lowest empty energy band is called the conduction band (CB). If the global minimum of the CB has the same wave vector, **k**, value as the global maximum of the VB in momentum space the semiconductor is said to have a *direct* band gap. If the **k** value differs the semiconductor is termed an *indirect-gap* semiconductor. In a direct-gap semiconductor an electron in the CB can fall to an empty state in the VB, giving off the energy difference E_g as a photon without a change in the electrons momentum. For a similar indirect-gap transition which involves a change in momentum, part of the energy is generally given up as heat to the lattice rather than as an emitted photon. Thus the photon emission efficiency in direct semiconductors is by far superior to indirect semiconductors, such as Si. All semiconductors studied in this work are direct. Typical band structures for direct and indirect semiconductors are illustrated in Figure 2.7:

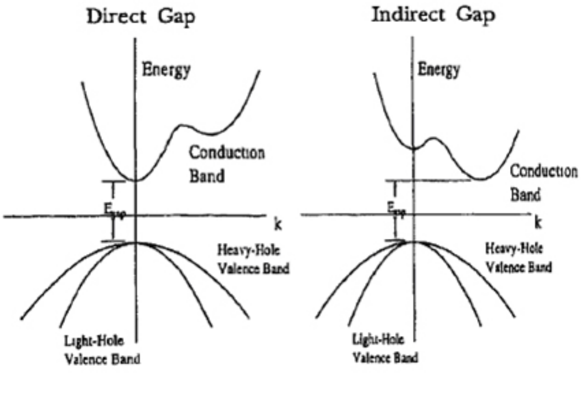

Figure 2.7: Typical dispersion relation (energy vs. wavevector **k**) for both direct(left) and indirect(right) semiconductors.

2.1.2 Surface states

The surface, in crystals defined as the two-three outermost atomic layers that differ significantly from the bulk, of any material is in fact a defect. At the surface there is no longer a periodic lattice, this leads to a different atomic bonding at the surface than in the bulk. Work is done on the system when atomic bonds are broken at the surface resulting in an accumulation of surface free energy. To reduce the surface free energy the outermost atomic layers rearrange themselves in a process of either *relaxation* or *reconstruction*. In relaxation the interlayer spacing at the top surface changes, usually reduces, while still maintaining the periodicity parallel to the surface and the symmetry of the surface. Reconstruction is a more extensive process where the surface periodicity, and in some cases even the surface symmetry, changes from the bulk.

Surface reconstruction often occurs in semiconductor materials where neighbouring atoms can share dangling bonds and thereby minimize the energy of the system. Note that planes in a crystal has different amount of surface free energy, for instance the fcc(111) plane has lower surface free energy than both fcc(100) and fcc(110). Generally a high surface atom density plane has less surface free energy and is therefore more stable.

Reconstruction can readily be detected with surface diffraction techniques like Reflection High Energy Electron Diffraction (RHEED) or Low Energy Electron Diffraction (LEED). The *Wood's* notation is most commonly used for surface reconstructions: GaAs(001) - (m x n)Rϕ, translates to a GaAs crystal oriented with the [001] direction normal to the surface having a surface structure (due to reconstruction) with a unit mesh that is $m\ x\ n$ times larger than the underlying bulk structure and is rotated with an angle ϕ. Both relaxation and reconstruction leads to a number of extra electronic states in the bandgap near the surface different materials.

To visualize the influence surface states has on the bandgap in two dimensions, the surface and bulk can be treated as two separate materials brought into contact with each other, see Figure 2.8a.

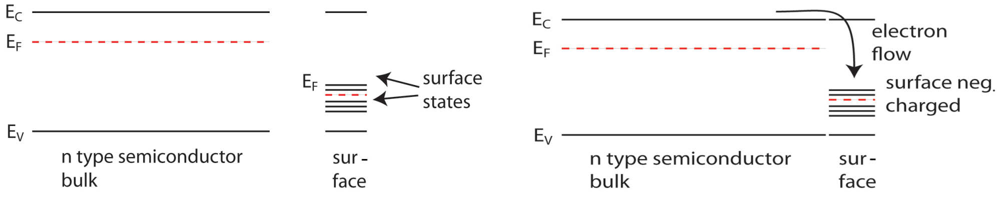
E$_C$
E$_F$
E$_F$
surface
states
E$_V$
n type semiconductor
bulk
sur -
face
E$_C$
E$_F$
electron
flow
surface neg.
charged
E$_V$
n type semiconductor
bulk
sur -
face

(a) (b)

Figure 2.8: (a) A n type semiconductor bulk with its surface when treated as separate materials. (b) Electrons flow from the CB to empty states at the surface.

For simplicity the surface is pictured with the same band diagram as the bulk. The surface adds a number of new states in the previously forbidden bandgap and when the surface and bulk comes into contact, electrons from the CB will immediately start to flow to the empty states of the surface, Figure 2.8b. This leads to an additional negative charge on the surface which in turn leads to an increase in the electrostatic potential there. This so-called band bending can be seen in Figure 2.9a.

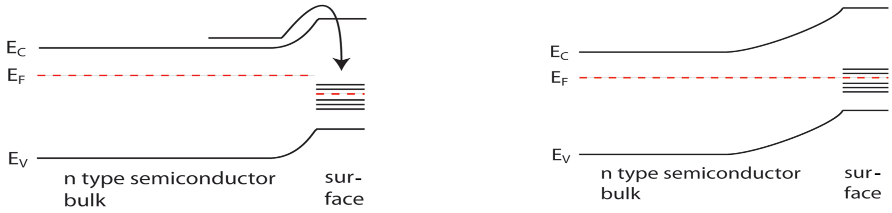
E$_C$
E$_F$
E$_V$
n type semiconductor
bulk
sur-
face
E$_C$
E$_F$
E$_V$
n type semiconductor
bulk
sur-
face

(a) (b)

Figure 2.9: (a) The VB and CB bends upwards because of the increase in electrostatic potential at the surface. (b) Here the Fermi level of the bulk matches the Fermi level of the surface (i.e. we have equilibrium).

The flow of electrons to the surface (and increase in potential) will continue until equilibrium is reached, i.e. when the Fermi level of the bulk matches the Fermi level of the surface, see Figure 2.9b. In a sense the surface states pins the Fermi level to a certain value for the entire material.

Several models for explaining the Fermi level pinning phenomenon exists like the unified defect model (UDM) [19] [20], the metal-induced gap state (MIGS) model [21] [22], the disorder-induced gap state (DIGS) model [23] and the effective work function (EWF) model [24]. There is still no unified model comprehensive enough to satisfactory explain the phenomenon but the bottom line is that a high density of surface states leads to a strong Fermi level pinning resulting in a high number of electron-hole recombinations centres at the surface. For NWs the surface states are very influential for the overall performance due to their high surface-to-volume ratio. The result is that a lot of the energy input on NWs is lost as heat because of a large number of non-radiative electron-hole recombinations at the surface.

2.2 GaAs/AlGaAs core-shell heterostructures

Growth of nanoscale materials with MBE allows for a very high level of precision, even down to a single atomic layer. Heterostructures, which consist of two or more materials, can be fabricated by changing the alloy composition during growth. GaAs/AlGaAs core-shell NWs consists of a GaAs core coated with an AlGaAs layer. GaAs has a direct bandgap, high carrier mobility and a high drift velocity and is therefore a very attractive semiconductor compound for use within nanoscale optoelectronic devices. A problem with GaAs is weak luminescence at room temperature because of its high surface state density, a problem that becomes very significant for NWs because of their high surface to volume ratio. To adress this issue the GaAs cores can be coated by a *passivation layer* to prevent non-radiative recombinations at the surface and thereby improve the radiative properties of the material. AlGaAs works well with GaAs because the lattice mismatch between the compounds is low (~0.12%) and the bandgap difference is high (~0.74 eV)[25]. AlGaAs also has a direct bandgap up to an Al content of around 45%, a characteristic which is especially important within optoelectronics. A high bandgap difference between the core and shell produces an effective potential barrier for carriers moving along the NWs and thus makes it less likely for those carriers to be trapped by non-radiative surface states. When two different compounds are put together a lattice mismatch is unavoidable, the lattice mismatch leads to interface states which leads to non-radiative trapping of carriers, much like the surface state problem discussed in section **??**. A low lattice mismatch gives a low interface state density and the "trade-off" with adding a passivation layer is minimized. *Strain* which can lead to drastic changes in the band structure [26] is also reduced when the lattice matching between the materials is good. In Figure 2.10 a plot of lattice constant of some common semiconductors against their bandgap minimum shows the close lattice matching of GaAs and AlAs.

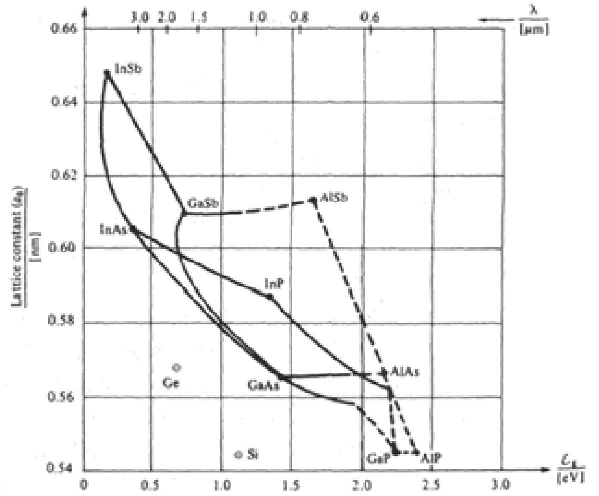

Figure 2.10: Lattice constant as a function of the bandgap minimum for some common semiconductors.

GaAs/AlGaAs core-shell NWs has shown great improvement over 2D and bulk systems in carrier mobility [27] and this system also has a low threshold current which makes it a good candidate for use as a laser. Adding AlGaAs shells around the GaAs NW cores has been reported to improve the luminescence from 20 up to 200 times compared to GaAs NWs without shell [28] [29].

2.2.1 Band structure of GaAs/AlGaAs core-shell NWs

The bandgap of $Al_xGa_{x\text{-}1}As$ at room temperature is given by [30]:

$$\text{For x<0.45: } E_g = 1.424 + 1.247x \text{ eV}, \tag{2.2}$$

$$\text{for x>0.45: } E_g = 1.9 + 0.125x + 0.143x^2 \text{ eV}. \tag{2.3}$$

For GaAs the band gap at room temperature is 1.424 eV [31]. The band discontinues at each $Al_xGa_{1\text{-}x}As$/GaAs interface is given by [30]: For the valence band (VB):

$$\Delta E_v = 0.46x \text{ eV}. \tag{2.4}$$

For the CB there are two equations depending on the composition of Al:

$$\text{If x<0.41: } \Delta E_c = 0.79x \text{ eV}, \tag{2.5}$$

$$\text{and if x>0.41: } \Delta E_c = 0.475 - 0.355x + 0.143x^2 \text{ eV}. \tag{2.6}$$

This gives a very simplified and ideal bandgap structure for GaAs/AlGaAs core-shell NWs when viewed from the side shown in Figure 2.11, here with an Al content of 33%. This is known as a type-I c band structure [32] where a material with higher bandgap surrounds a material with lower band gap.

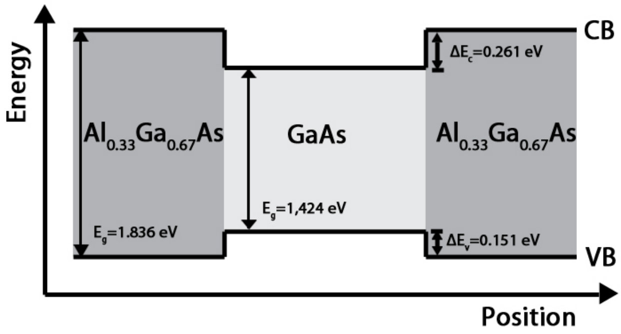

Figure 2.11: Band structure of AlGaAs/GaAs/AlGaAs sandwich for an Al composition of 33%. The ratio between the CB offset and the VB offset is here approximately 79/46.

As stated this is a very simplified illustration where neither surface states, band bending nor strain is considered.

The bandgap of any material is temperature dependent. For AlGaAs with an Al content lower than 45% the temperature dependence on the bandgap is given by:

$$E_\Gamma = E_\Gamma(0) - \frac{5.405 \cdot 10^{-4} T^2}{(T + 204)} \text{ eV}, \tag{2.7}$$

where $E_\Gamma(0) = 1.519 + 1.155x + 0.37x^2$ eV.

For GaAs the temperature dependence is given by:

$$E_\Gamma = 1.519 - \frac{5.405 \cdot 10^{-4} T^2}{(T + 204)} \text{ eV}. \tag{2.8}$$

These equations are taken from [30]. A more thorough look at the temperature dependency on the bandgap for common semiconductors and alloys can be found in [33] where a number of different research findings on the subject are summarized.

It is important to note that the Al content in NWs have been shown to vary along their length with the highest percentage of Al at the NW base and then decreasing towards the top of the NWs [34]. Overall the Al content in AlGaAs NWs has been found to be less than in conventional AlGaAs 2D thin films and as a consequence AlGaAs NWs have a smaller bandgap than its 2D film counterpart. The change in Al content can be attributed to the difference between VLS/VS growth and 2D film growth. VLS and VS growth is highly dependent on the diffusion length of the species involved, and the decreasing Al content with NW height is a result of Al having a lower diffusion length than Ga (this is discussed further in section 2.4. For instance in *Growth and photoluminescence characteristics of AlGaAs nanowires* by Wu et al.[35] they found that AlGaAs NWs had an Al content of 13% while their reference AlGaAs 2D film had an Al content of 24% (i.e. 46% less Al in the NWs).

A useful technique for studying the band structure of different materials is photoluminescence (PL). This technique uses laser light to optically excite electrons in a given sample. After a short time (normally in the order of picoseconds) the electrons return to their equilibrium states and the energy gained is released either as photons (radiative recombination) or as phonons (non-radiative recombination). PL is the study of photons emitted from this process and it gives information about the band gap, impurities and defects, composition, recombination mechanisms and material quality of the sample material. Figure 2.12 illustrates a simple but typical radiative recombination in the GaAs/AlGaAs system.

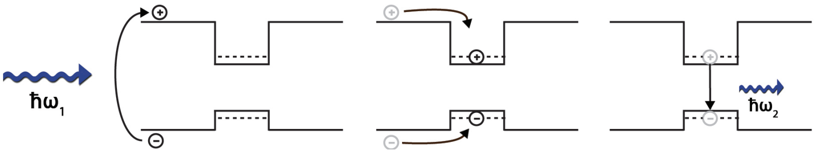

Figure 2.12: Illustration of a raditive recombination in a type I-c bandstructure, here with GaAs sandwiched between two AlGaAs segments.

A photon with energy $\hbar\omega_1$ enters the AlGaAs shell on the left and excites an electron from the VB to the CB resulting in the creation of a hole in the VB. The Coulomb attraction between the electron and hole, due to their opposite charges, forms a bound state called an *exciton*. The strength of the Coulomb attraction depends on the material but for semiconductors this force is relatively weak because of a high dielectric constant. This results in an exciton with a much higher radius than the lattice spacing, known as a *Wannier* exciton, and a binding energy in the order of only 0.01 eV. To lower its potential the exciton moves from the AlGaAs layer and the electron (hole) relaxes at the bottom (top) of the CB (VB) in the GaAs core. If the lowest states are filled the electron and hole will relax to the next available state, obeying the Pauli principle, in what is known as a *state filling effect*. The electron now recombines with the hole simultaneously emitting a photon with energy $\hbar\omega_2$. This is known as a band-to-band recombination and is only one of many possible radiative recombination mechanisms some of which are illustrated in Figure 2.13. Also in addition to the exciton there exists many other species of many-particle states such as biexcitons, excitonic molecules, electron-hole plasmas and electron-hole liquids [36].

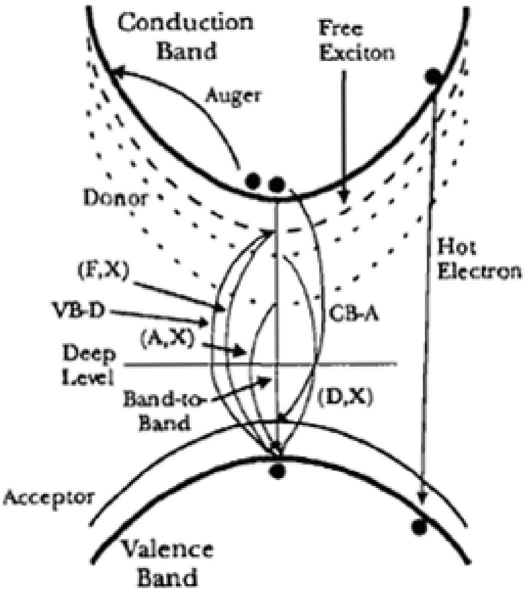
Conduction Band
Free Exciton
Auger
Donor
Hot Electron
(F,X)
VB-D
CB-A
(A,X)
Deep Level
Band-to-Band
(D,X)
Acceptor
Valence Band

Figure 2.13: Illustration of some possible radiative recombination processes from [36]. **Auger** recombination is a non-radiative three-body process where the energy from the recombination is transferred to another particle as kinetic energy. Electrons (holes) that have not relaxed to the bottom (top) of the CB (VB) before they recombine are known as **hot carriers**. A radiative recombination of a free carrier with a carrier bound to an impurity is here denoted **VB-D**, for donor-to-valence band, and **CB-A** for conduction band-to-acceptor recombination. Excitons that become bound at donors or acceptors are denoted as **(D,X)** and **(A,X)** respectively and results in subband emission. Recombination via an intermediary state (i.e. deep level) has been termed Shockley-Read-Hall recombination, and is primarily non-radiative in nature.

2.3 Density Of States

If the thickness of the GaAs core, in the GaAs/AlGaAs system, is less than the de Broglie wavelength of the carriers, which is around 20 nm for electrons in GaAs, the carriers are confined to move in only two spatial dimensions parallel to the GaAs-AlGaAs interfaces and carrier movement in the direction perpendicular to the interfaces is restricted. This is known as *quantum confinement* and it causes large changes in the dispersion relation of the *density of states* (DOS) for free carriers. The DOS of a system describes the number of states at each energy level that are available to be occupied. If a structure restricts carrier movement to two dimensions (2D) it is known as a *quantum well* (QW), further restrictions to one dimension (1D) and zero dimensions (0D) are denoted *quantum wires* (QWRs) and *quantum dots* (QDs) respectively. The reduced dimensionality in these structures increases the Coulomb interaction between electron and holes; for instance in a 2D system the exciton binding energy is four times as strong as in a 3D system. Figure 2.14 illustrates the degree of confinement for structures of different dimensionality and the DOS associated with them.

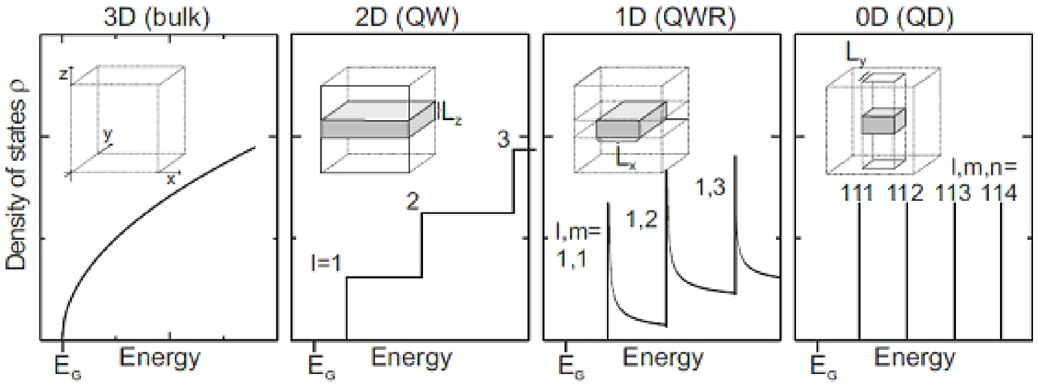

Figure 2.14: DOS for bulk (3D) and low dimensonality (2D, 1D and 0D) semiconductor structures.

2.4 Growth mechanisms

Fabrication of GaAs/AlGaAs core-shell NWs involves two types of growth mechanisms; vapor-liquid-solid (VLS) and vapor-solid (VS) growth. The GaAs cores made in this experiment grew mainly by the VLS mechanism while the AlGaAs shells showed both types of growth.

2.4.1 Vapor-Liquid-Solid (VLS) growth

The VLS growth mechanism was first proposed by Wagner and Ellis [37] in 1964 and has since been widely accepted as the primary growth mechanism for free standing V-III semiconductor NWs. The VLS growth mechanism can be described in the following steps:

1. A catalyst metal, usually gold, is deposited on a semiconductor substrate (e.g. GaAs(111)B) either as nano particles or as a thin film.

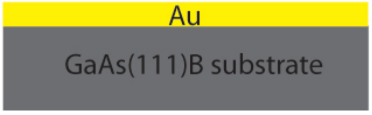

Figure 2.15: Thin film of Au on GaAs(111)B substrate.

2. The substrate temperature is increased above the eutectic melting point and droplets of liquid Au-Ga alloy are formed. The diameter of these droplets range from 10 to 100 nm depending on the thickness of the deposited Au layer. Thicker Au layer results in larger droplets. Au normally melts at 1064 °C but for the Au-Ga alloy the melting point can be as low as 339 °C [38].

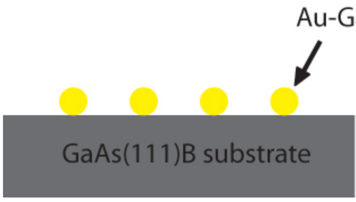

Figure 2.16: Au-Ga liquid alloy droplets on top of a GaAs(111)B substrate.

3. Additional semiconductor material in vapor phase is deposited on the surface (in this example Ga and As). The Au-Ga droplets become supersaturated when hit by deposit atoms, meaning that the chemical potential becomes lower at the droplets than in the vapor. Atoms hitting the droplets will either re-evaporate or freeze out from the liquid droplets forming a solid NW beneath them. The liquid-solid interface acts as a sink for deposit atoms dissolved in the drop, causing them to incorporate into the available adsorption sites of the lattice. Deposit atoms that lands either on the sidewalls of the NWs or on the substrate itself (called *adatoms*) can diffuse along the sidewalls to the drop and thereby contribute to the growth of the NWs. A number of the atoms hitting the substrate surface will not diffuse along the NWs; instead they will coalesce on the surface thus forming a growing 2D layer. For NW lengths below the adatom diffusion length for a particular growth material the diameter of the NWs will be equal to the diameter of the Au-Ga droplets.

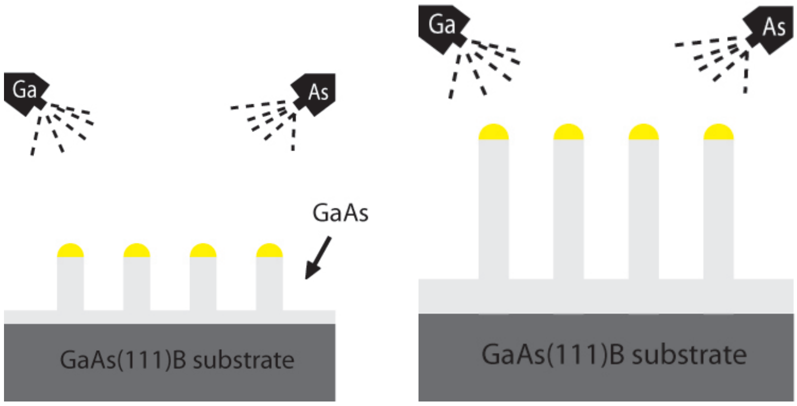

(a) (b)

Figure 2.17: (a) GaAs(111)B substrate with deposition of Ga and As. Here the NWs has started to grow. Note that there is also considerable growth of a 2D layer at the surface. (b) The NWs keep growing in the axial direction with the continued deposition of Ga and As.

2.4.2 Vapor-Solid (VS) growth mechanism

VS growth differs from VLS growth in that there is no liquid element directly involved in the process. In VS growth the deposited atoms does not enter the liquid Au-droplets instead they nucleate on the substrate surface or on the sidewalls of previously grown NWs. The growth of AlGaAs shells coating GaAs NW cores starts out as VLS growth in the axial direction but as the length of the NWs becomes longer than the Al adatom diffusion length the growth shifts to radial dominated (i.e. VS growth is initiated). Now many of the atoms landing on the sidewalls of NWs will not have the sufficient diffusion length needed to reach the liquid droplet. Instead they will start to nucleate on the sidewall surface forming a layer by layer epitaxial growth in the radial direction. Depending on where the atoms hit on the NW sidewalls they can migrate up towards the liquid droplet, down towards the NW base or to the substrate surface. Atoms hitting the substrate directly can as before diffuse to the NW sidewalls but will not reach all the way to the liquid droplet. Atoms hitting the liquid droplet directly will as before, given they are not re-evaporated, experience a VLS growth and contribute to axial growth. The number of atoms directly hitting the liquid droplets is very few so the growth in the axial direction is negligible.

The reason for the difference in growth for GaAs and AlGaAs is that Al is an active atom, which means that the Al adatoms (~1.74 eV for AlAs grown on AlAs (001)) will have a higher effective surface diffusion barrier compared to Ga adatoms (~1.58 eV for GaAs grown on GaAs (001)) [39, 40]. This in turn leads to a diffusion length of Al that is at least a factor 4 lower compared to Ga and VS growth is initiated at a much earlier stage for AlGaAs than for GaAs. If the diffusion length of Ga on a (111)B surface is 10 μm at a temperature of 580 °C as found in [41] the Al diffusion length would be less than 2.5 μm under the same conditions. An illustration of the actual growth of an AlGaAs shell, surrounding a GaAs NW core, with both VLS and VS growth can be seen in Figure 2.18.

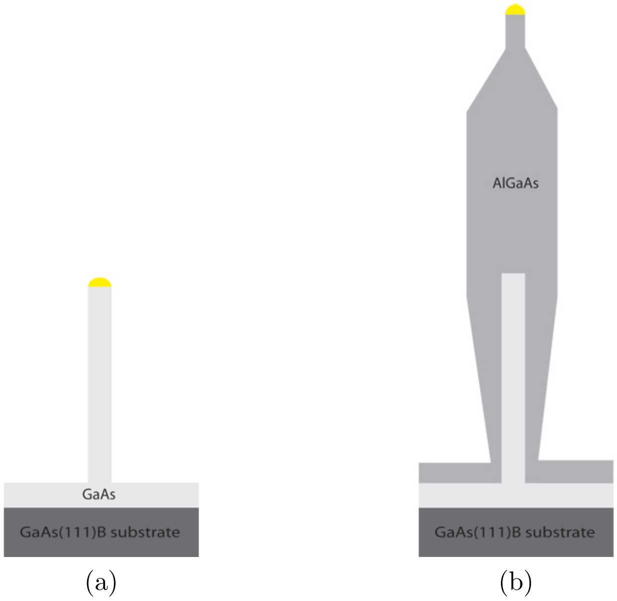

(a) (b)

Figure 2.18: (a) Free standing GaAs NW on a GaAs(111)B substrate. (b) GaAs/AlGaAs core-shell NW on a GaAs(111)B substrate. The growth of the AlGaAs shell goes from axial to radial dominated when the length of the wires exceeds the Al diffusion length.

2.4.3 Diffusion induced growth model

The diffusion of adatoms plays an important part in the growth of semiconductor NWs by MBE. A recent growth model introduced by Dubrovskii [42, 43] incorporates diffusion with the VLS growth mechanism. To better identify the problem the following assumptions are made in Dubrovskii's growth model:

- All atoms arriving at the drop, irrespective of their pathway to it, are first dissolved in the drop and then either re-evaporate or attach to the crystal lattice.
- The supersaturation of liquid alloy in the drop ζ, the drop radius R and all other characteristics of the growth process vary with time.
- The number of catalyst particles remains constant during the growth.
- The liquid alloy drop is hemisphere with a radius R.

- The catalyst and deposit atoms occupy the same volume Ω_l in the liquid phase.

Further all the processes taking place at the growth site are schematized in Figure 2.19:

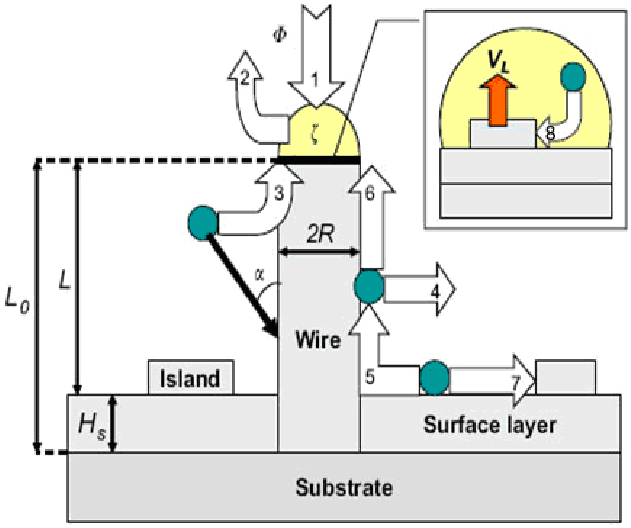

Figure 2.19: Growth processes at the growth site.

1. Atoms directly hitting the drop.
2. Atoms that first dissolve in the drop and then re-evaporate to the surroundings.
3. Atoms hitting the sidewalls of NWs and then diffuse to the drop.
4. Desorption of atoms from the sidewalls.
5. Diffusion from the substrate to the sidewalls.
6. Diffusion from the substrate along the sidewalls to the drop.
7. Nucleation and lateral growth of 2D islands on the substrate surface.
8. Nucleation-mediated growth from the liquid alloy on the NW top.

The governing factor for VLS growth is the supersaturation of liquid alloy in the drop (the chemical potential difference between the liquid drop and its surroundings). The relationship between the NW radius R and the supersaturation of liquid alloy in the drop ζ is given by:

$$R = \frac{R_0}{[1 - \chi_{\mathrm{eq}}(\zeta + 1)]^{\frac{1}{3}}} \tag{2.9}$$

Where $R_0 = N_0\Omega_{\mathrm{l}}$ is the radius of the catalyst drop when there is no deposit atoms present in the drop, N_0 is the number of catalyst atoms (e.g. Au) in the drop, Ω_l is the volume of a catalyst atom in liquid phase and χ_{eq} is the equilibrium concentration of catalyst and deposit atoms in the drop. The supersaturation can be expressed as $\zeta = \chi/\chi_{\mathrm{eq}} - 1$ where χ is the concentration of deposit atoms in the alloy. If the adatom diffusion length L_f is much larger than the length L of the NWs and if we assume that the drop radius R is independent of time the steady-state equation for the length of NWs L is given by:

$$\frac{\mathrm{d}L}{\mathrm{d}t} = V_0(\Phi - \zeta) - (1 - \epsilon)V + V\frac{R_1}{R\cosh(\lambda)} \tag{2.10}$$

Here $V_0 = V/(\Phi+1)$ where V is the deposition rate and Φ is the supersaturation of the gaseous phase. $\epsilon = (V - V_s)/V$ is the relative difference between the deposition rate and the growth rate of the substrate surface V_s. $R_1 = \epsilon/(\pi < R > N_w)$ is a parameter describing the diffusion-induced contribution, $< R >$ is the mean base diameter of the NW array and N_w is the surface density of the NW array. $\lambda = L/L_f$ is the ratio of whisker length L to the adatom diffusion length on the sidewalls, $L_f = \sqrt{D_f\tau_f}$, D_f is the corresponding diffusion length and τ_f is the mean lifetime of adatoms on the sidewalls. If also the diffusion flux of adatoms from the sidewalls is much larger than the deposition flux V then $R_1/R\cosh(\lambda) \gg 1$ and equation 2.10 simplifies to:

$$\frac{\mathrm{d}L}{\mathrm{d}H} = \frac{R_1}{R\cosh(\lambda)} \tag{2.11}$$

Where $H = V_t$ is the effective thickness of deposited material. Here the contributions from adsorption and desorption and the influence of substrate growth is negligible. With the initial condition $L(H=0)=0$ the solution of equation 2.11 is:

$$\sinh(\frac{L}{L_f}) = \frac{R_1 H}{R L_f} \tag{2.12}$$

And we end up with the very simple equation for the length of NWs when $\lambda \gg 1$:

$$L = \frac{R_1}{R} H \tag{2.13}$$

If the supersaturation of the gaseous phase Φ is very high, which is the case with growth of NWs by MBE, regardless of the values of R_1 and λ, equation 2.10 is reduced to:

$$\frac{\mathrm{d}L}{\mathrm{d}H} = \epsilon - \gamma + \frac{R_1}{R\cosh(\lambda)} \tag{2.14}$$

Where $\gamma = V_0/V$ is a coefficient that accounts for the desorption contribution. For $\gg 1$ the integration of equation 2.14 gives:

$$L = (\epsilon - \gamma + \frac{R_1}{R})H \tag{2.15}$$

Equation 2.15 is a very good approximation for thin NWs. Diffusion-induced growth is the main contribution to NW growth when the drop radius is small and the length of NWs decreases when the wire radius increases for this type of growth.

Chapter 3

Materials and Methods

3.1 Materials

This section gives a brief description of the equipment used in this project.

3.1.1 Molecular Beam Epitaxy (MBE)

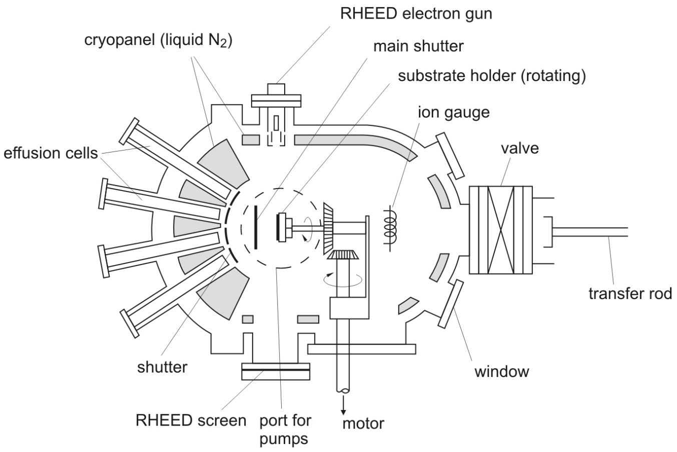

RHEED electron gun
cryopanel (liquid N_2)
main shutter
substrate holder (rotating)
ion gauge
effusion cells
valve
transfer rod
shutter
window
RHEED screen
port for pumps
motor

Figure 3.1: Schematic drawing of MBE growth chamber.

MBE is used for growing thin epitaxial structures in a thermally controlled and ultra-high vacuum chamber. Source elements such as Ga, As, Al, In, Sb, Si, Te and

Be are heated within crucibles known as *Knudsen* cells and deposited as molecular beams onto a heated substrate. The deposition is controlled by mechanical shutters. MBE has a relatively slow growth rate, about one monolayer per second that enables very abrupt hetero-junctions to be formed. Temperature control, deposition rate and high vacuum are key elements in MBE. Ultra-high vacuum (around 10^{-10} Torr) is achieved with pumps and by cooling the cryopanels surrounding the growth chamber with liquid nitrogen. MBE growth is mainly governed by kinetics at the substrate surface and there are no collisions or chemical reactions between the particles in the molecular beams before arriving at the surface. A great advantage with MBE is the possibility to use *in-situ* monitoring during growth such as *Reflection High Energy Electron Diffraction* (RHEED).

RHEED can be used to determine surface reconstruction, growth rate and when the oxide has desorbed from the wafer. A high energy electron beam ranging from 5 to 40 keV is directed at a low angle (1-3°) to the surface. The beam is diffracted at the sample surface and hits a cathodoluminescent screen where the diffraction pattern is detected by a CCD camera. The diffraction pattern gives information about the reconstruction on the substrate surface. The growth rate of the surface can be found by measuring the specular beam intensity. As an example the specular beam intensity variations during growth of GaAs(001) [44] is shown in Figure 3.2. The specular beam intensity oscillates because of the repeated formation of bi-atomic Ga-As layers. Each local maximum of the intensity oscillations corresponds to the completion of a new GaAs layer. In this manner the growth rate can easily be determined and the thickness of different growth layers can be controlled by a high level of precision. During this project a Varian Gen II Modular MBE was used.

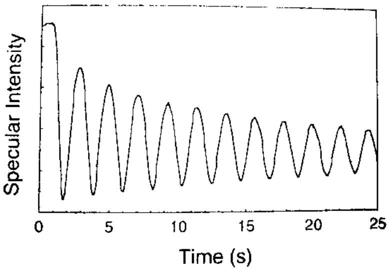

Figure 3.2: Specular RHEED intensity oscillations from a singular GaAs(001) at a temperature near 575 °C.

3.1.2 Secondary Electron Beam (SEM)

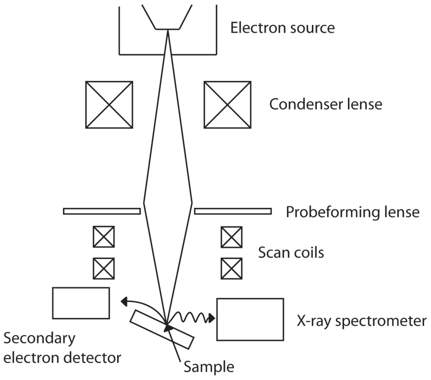

Figure 3.3: Schematic drawing of SEM mode of operation.

An electron beam is focused on a tiny spot and then scanned over the sample surface in a raster pattern. The beam has an energy ranging from a few hundred to fifty thousand electron volts. While the electron beam is scanning the sample, secondary electrons and elastically backscattered primary electrons are captured by a detector. The number of electrons detected on the various areas on the sample surface makes up the contrast in the image. An elevated area on the surface gives a higher number of scattered electrons. The interaction between the incoming electron beam and the sample takes place in a drop-shaped area with a depth of approximately one micrometer. This means that SEM only gives an image of the sample surface. With conventional SEM magnifications up to three hundred thousand times the original size is possible and with very advanced types of SEM the magnification is even higher. Imaging with SEM requires a high vacuum of around 10^{-6} Torr. The resolution in the image is determined by a combination of how well the electron beam is focused on the sample surface, the intensity of the beam (affects the signal-to-noise ratio at the detector), and how good the detector is. SEM normally gives resolutions down to around one nanometer. SEM is mostly used for studying conductor and semiconductor surfaces when higher resolution than an optical microscope can give is required.

In this project a Low Voltage Field Emission SEM (LVFeSEM) Zeiss Supra 55 VP (variable pressure) and a FeSEM Zeiss Ultra 55 Limited Edition was used.

3.1.3 Transmission Electron Microscopy (TEM)

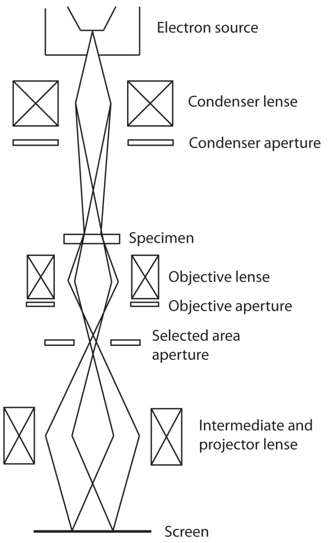
Electron source
Condenser lense
Condenser aperture
Specimen
Objective lense
Objective aperture
Selected area aperture
Intermediate and projector lense
Screen

Figure 3.4: Schematic drawing of TEM mode of operation.

A beam of electrons focused by electromagnetic lenses is transmitted through a very thin sample (around 100 nm). The electron beam has an energy ranging from 10 to 1000 keV and is produced by heating a tungsten filament. A vacuum of around 10^{-4} to 10^{-8} Torr is achieved in the TEM with various pumps and nitrogen cooling. The contrast in the image comes from variations in the atomic composition or thickness of the sample which produces changes in the electron scattering from the main beam. TEM can also be used to study the crystallographic structure of solids by adjusting the intermediate lens so that the back focal plane of the objective lens is imaged at the object plane of the projector lens. A crystalline sample will give strong Bragg diffraction of the electron beam in specific direction and sharp spots will form in the focal plane of the objective lens. The two most common operation modes of a TEM are bright- and dark-field imaging. In bright-field image mode the direct electron beam (000) passes through the objective aperture. Grains or crystallites which are oriented along the zone axis will appear dark on a bright background. They appear dark because a large part of the beam which passes through them is Bragg scattered and stopped by the objective aperture. In dark-field image mode the objective aperture is centered on one or more of the Bragg scattered beams and only they contribute to the contrast in the image. Grains and crystallites appear bright on a dark background. Dark field imaging can give information about particle sizes and planar defects in the sample. The very short wavelength of electrons gives high image resolution. With conventional TEM magnifications up to one million times the original size is achieved giving resolutions down to a few Angstroms.

In this study a JEOL 2010F TEM (200 kV) with a scanning TEM (STEM) unit (1 nm probe, Cs =1 mm) was used.

3.1.4 Photoluminescence (PL)

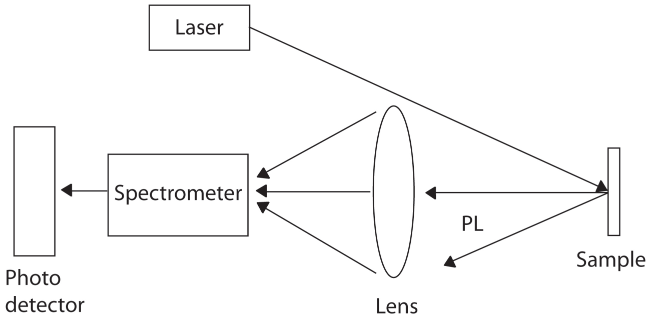

Figure 3.5: Schematic drawing of PL setup mode of operation.

Light from a laser is directed onto a sample and electrons in the sample are optically excited to higher energy states. When the excited electrons return to their equilibrium states the excess energy is released either as photons (radiative recombination) or as phonons (non-radiative recombination). If the excess energy is released as photons the process is known as photoluminescence (PL). In *low-temperature PL* (4-77K) the process is more complex with zero dimension (point) defects and electron-phonon interactions. With PL very narrow peaks can be obtained in an intensity spectrum, especially for low-temperature PL, which make analysis possible. The emitted photons give information about the band gap, impurities and defects, composition, recombination mechanisms and material quality of the sample material. In order to excite electrons the incoming light must have an energy that is higher than or equal to the bandgap of the sample material. The energy of the incoming light is determined by its wavelength and is approximately equal to $1240/\lambda$ eV where λ is the wavelength in nanometers. PL is a simple, versatile and non-destructive technique with minimal sample preparation. A drawback with PL is that it relies entirely on radiative events which make low-quality indirect bandgap semiconductors difficult to study.

In this study a Attocube CFMI was used with a 532 nm laser line as excitation source, dispersed by a Jobin-Yvon spectrometer and detected by a thermal electric cooled Andor Newton Si charge-coupled device camera.

3.2 Methods

3.2.1 Growth Procedure

In this experiment two GaAs/AlGaAs core-shell NW samples were grown on GaAs(111)B substrates with a Varian Gen II Modular MBE, metalized with an e-beam evaporator and characterized with SEM and low temperature μ-PL. Sample A consisted of a GaAs core grown for 25 minutes and an AlGaAs shell with 33% aluminium grown for 15 minutes. Sample B also had a GaAs core which was grown for 25 minutes but the AlGaAs shell of this sample had an aluminium content of 50% and was grown for 7 minutes. After deoxidizing the substrate surface at 620 °C a buffer layer was grown. The buffer consisted of a 60 nm thick GaAs layer followed by a 72 nm thick AlGaAs marker and lastly a 36 nm thick GaAs layer. The marker layer is necessary to be able to measure the height of the 2D layer with SEM. The temperature during buffer growth was 620 °C and the As flux was kept at $9 \cdot 10^{-6}$ Torr which gave a $\sqrt{19} \cdot \sqrt{19}$ surface reconstruction resulting in an atomically flat surface. The planar growth rate of Ga and Al was 2 Å/s (0.7 ML/s) and 1 Å/s (0.35 ML/s) respectively.

The sample was then transferred out of the MBE and an Au layer of 2 Å was deposited on top of the buffer with an electron beam evaporator and the sample was again transferred back into the MBE growth chamber. Under an As_4 flux of $6 \cdot 10^{-6}$ Torr the substrate temperature was increased to 545 °C, a temperature suitable for GaAs NW growth, leading to the formation of Au-Ga liquid alloy droplets on the surface.

The fabrication of the GaAs/AlGaAs core-shell structures consisted of three growth steps:

- First the GaAs cores was constructed by opening the Ga effusion cell, preset to yield a Ga planar growth rate of 2 Å/s (0.7 ML/s), resulting in vertical growth of GaAs NWs. The GaAs NW cores were then grown for 25 minutes.
- Secondly the growths of the AlGaAs shells cladding each GaAs NW core were initiated by opening the Al effusion cell. For sample A the Al planar growth rate was pre-calibrated to give an $Al_{33}Ga_{67}As$ (33% Al) shell composition

while for sample B the shell consisted of $Al_{50}Ga_{50}As$ (50% Al). It should be noted that the Al/Ga composition calibration which was done on a 2D-film differs from the Al/Ga composition in the resultant NWs. The percentage of Al in the final NWs are lower than expected from the calibration, this alteration from 2D-film to NW in AlGaAs composition is fruther discussed in section 2.2.1 of the *Theory* chapter. For sample A with 33% Al content the AlGaAs shell was grown for 15 minutes, while for sample B which had 50% Al content the AlGaAs shell was grown for 7 minutes.

- After the shell growth was terminated by turning off the Al shutter a very thin GaAs cap was grown for 5 minutes at 450 °C with an As_2 flux of $6 \cdot 10^{-6}$ Torr for both samples. The purpose of the GaAs cap is to prevent oxidation of the AlGaAs shell when exposed to air.

3.2.2 Structural characterization

For both samples statistical information about length, diameter and density was gathered by analyzing images taken with SEM. One hundred NWs, from randomly chosen areas of the samples, were investigated for each sample. The length of the NWs was measured from the kink (were the 2D layer ends) and to the top of the Au particle as can be seen in Figure 3.6. The tapering length (the distance from the top of the NWs to where tapering begins) was also measured. Diameters were measured at the top, centre and base of the NWs. The density of the NWs was found from taking random top view images in SEM and then counting the number of NWs in an area of 1 μm^2. The height of the 2D layers were also investigated using SEM and an example of that is shown in Figure 3.7.

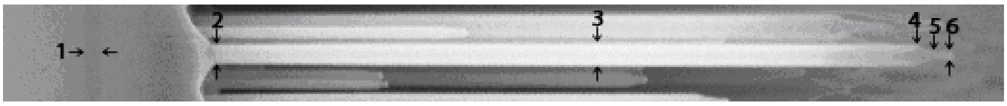

Figure 3.6: Example of the measurements done on the NWs in this study. (1) Thickness of Al marker, NW diameter at the bottom (2), centre (3) and top (6). The start and end of tapering at the NW tops is indicated with (4) and (5) respectively. The length of the NWs was measured from the kink (at (2)) and to the top of the Au particle (at (6)).

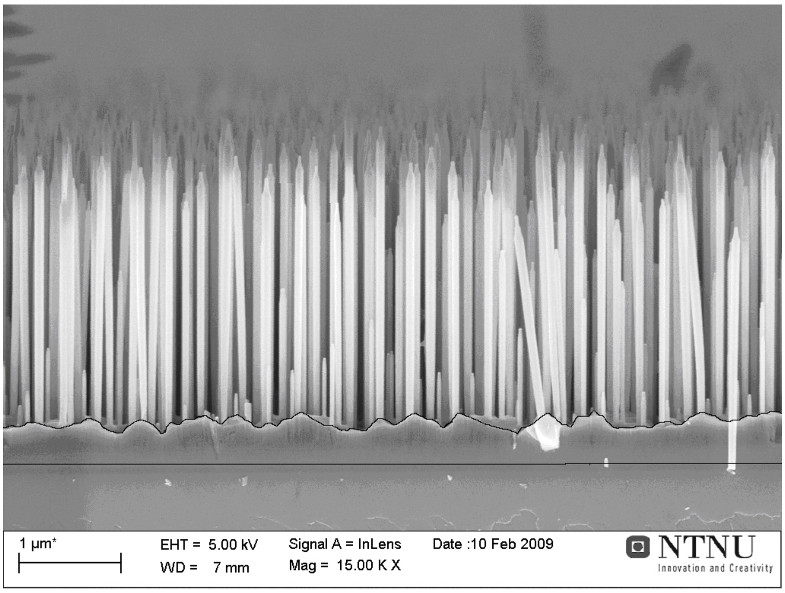

Figure 3.7: Example of 2D layer measurement from sample A. The area of the 2D layer was measured and then divided by the length to find the average height. Notice the AlGaAs marker appears as a dark line in the image which is necessary to distinguish the substrate from the 2D layer.

3.2.3 Optical Characterization

The optical properties of the NWs from the samples were investigated by low temperature μ-PL. Before the NWs could be analyzed they first had to be detached from the substrate, this was done by placing a small piece of the sample in a container with ethanol and sinking it in an ultrasonic bath for a couple of minutes. The detached NWs was then applied on a Cu grid which in turn was loaded in a cryostat containing liquid helium holding a temperature of 4.4 K. Single NWs were then excited by a 532 nm He cw laser. The laser was focused onto the sample using a 0.65 numerical aperture objective lens and a spot size of approximately 2 μm. The μ-PL from single NWs was dispersed by a 0.55 m focal length Jobin-Yvon spectrometer and detected by a thermal electric cooled Si CCD camera (Andor Newton). The spectral resolution of the system was ~200 μeV.

Chapter 4

Results and Discussion

4.1 Structural Characterization

In Figure 4.1 cross-sectional SEM images of the two GaAs/AlGaAs core-shell NW samples grown in this study are shown with equal length scales:

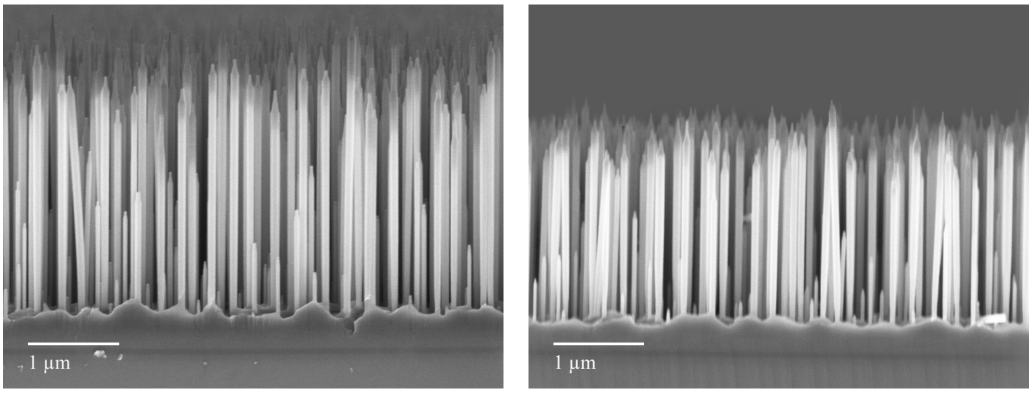

(a) Sample A: 33% Al in the shell. (b) Sample B: 50% Al in the shell.

Figure 4.1: Cross-sectional images of GaAs/AlGaAs core-shell NWs: (a) Sample A with GaAs core grown for 25 minutes and $Al_{0.33}Ga_{0.67}As$ (33% Al) shell grown for 15 minutes; (b) Sample B with GaAs core grown for 25 minutes and $Al_{0.50}Ga_{0.50}As$ (50% Al) shell grown for 7 minutes. The images were obtained with a Zeiss Supra field emission SEM (FE-SEM) operating at 5 kV with a working distance (WD) of 7 mm and a magnification of 15.00K. The images have equal length scales of 1 μm.

The samples were characterized with SEM to investigate the difference in morphology with Al content. Sample A consisted of a GaAs core grown for 25 minutes and an AlGaAs shell with 33% Al grown for 15 minutes. Sample B also had a GaAs core grown for 25 minutes but the AlGaAs shell for this sample had an Al content of 50% and was grown for only 7 minutes. The GaAs cores and AlGaAs shells for both samples were grown at a temperature of approximately 545 °C. All wires grew in the [111] direction normal to the surface which is the energetically preferred direction for GaAs NWs [45]. All wires also had a Au-droplet sitting at the top and this confirms that the NWs grew by a metal-assisted method described in section 2.4 of the *Theory* chapter. TEM measurents reveald that both samples had a WZ dominated crystal structure with a high number of stacking faults.

What is immediately clear from Figure 4.1 is that sample A on the left have NWs which are quite a bit longer than the NWs in sample B on the right, with the average NW length for sample A and B being measured to 2005 nm and 1781 nm respectively. What also can be seen in Figure 4.1 is that while most of the individual wires in both samples have approximately equal lengths, some of the wires are much shorter than others. In a MBE growth chamber the materials are deposited at an inclined angle (in this study: ~53°) and when the length of the wires increases some wires will shadow others and lower the amount of atoms directly hitting the shorter ones. This *shadowing-effect*, also experinced in [46], gets more and more pronounced as the wires become longer and the result is that some of the wires will end up much shorter than their neighbours.

Ideally we want the AlGaAs shell to grow only in the radial direction, cladding the entire length of the GaAs core with a uniform shell thickness. This was however not the case here, in both samples the shell grew in both axial and radial direction leading to a portion at the top (~1 μm) of the wires consisting of pure AlGaAs and to tapering of the wires at both top and bottom. The tapering towards the top of the NWs was more abrupt than the tapering towards the bottom which was more gradual along the length of the wires. Figure 4.2 gives a closer look at the top of the wires where tapering is clearly visible:

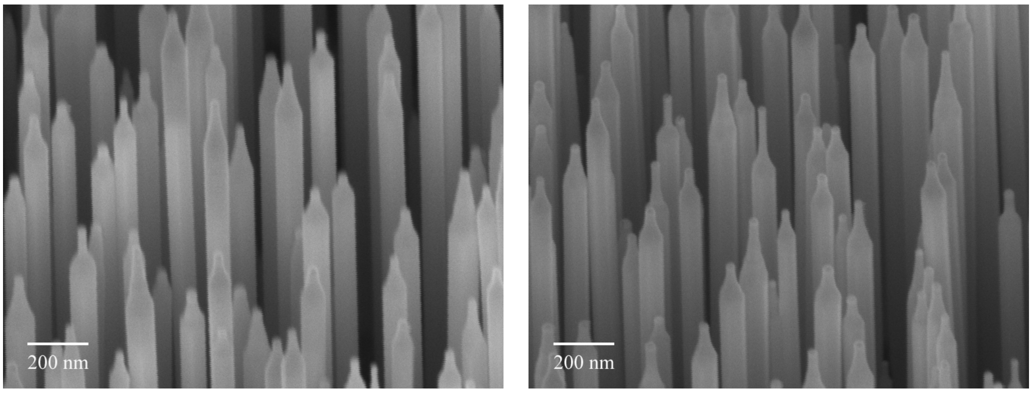
200 nm
200 nm

(a) (b)

Figure 4.2: Close-up of the top region of (a) sample A and (b) sample B taken at a 45° angle. Here tapering of the wires is clearly visible. The images were obtained with a Zeiss Supra field emission SEM (FE-SEM) operating at 5 kV with a WD of 9 mm and a magnification of 50.00K.

In Figure 4.3 the average values for 100 randomly picked NWs from both samples are illustrated:

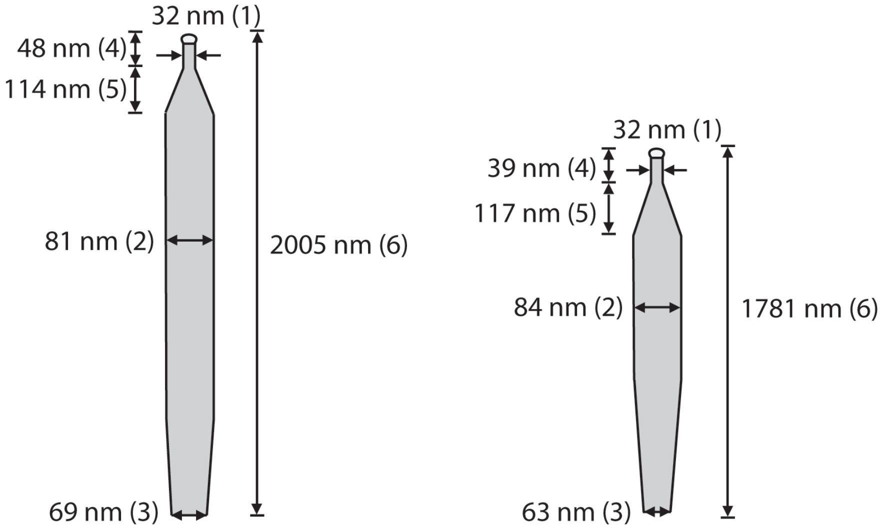
32 nm (1)
48 nm (4)
114 nm (5)
81 nm (2)
2005 nm (6)
69 nm (3)
32 nm (1)
39 nm (4)
117 nm (5)
84 nm (2)
1781 nm (6)
63 nm (3)

(a) (b)

Figure 4.3: Illustration of (a) sample A and (b) sample B with the average (1) top, (2) centre and (3) base diameters and the lengths of (4) the uniform segment at the top, (5) the tapered segment at the top and (6) the entire NW labelled.

The diameter of the wires varied quite a bit along the length of the wires and was therefore measured at three distinct places; at the bottom of the wires just above the kink, at the centre where the wires were fairly uniform, and at the top just below the Au droplet.

The base diameter for sample A was 69 nm while it was 63 nm for sample B. For the diameter at the centre it was 81 for sample A and 84 nm for sample B. For both samples the average top diameter was measured to 32 nm on average. Sample A had a 114 nm long tapered segment at the top of the wires on an average while this segment was 124 nm for sample B. Many of the wires had a uniform segment above the tapered region at the top, for sample A this segment was 48 nm long while it was 39 nm for sample B. The length from the tapering at the top started to the tip of the wires (tapered segment plus uniform segment) was 162 nm for sample A and 163 nm for sample B. The average height of the 2D layer was 372 nm for sample A and 311 nm for sample B.

The fact that the NWs from sample B with 50% Al in the shell on an average were 3 nm thicker at the centre of the wires than the NWs from sample A with 33% Al in the shell even though the shell in sample B was grown for 8 minutes less than the shell in sample A confirms that a higher Al content results in a lower diffusion length which in turn leads to a higher degree of radial growth for these particular compounds. It should be noted that the planar growth rate for the shell for sample A was higher than for sample B. For the shell growth the planar growth rate was calibrated to 1 Å/s for Al and 2 Å/s for Ga. This gave a planar growth rate of $1*0.33+2*0.67 = 1.67$ Å/s for the shell in sample A and $1*0.5+2*0.5 = 1.5$ Å/s for the shell in sample B. In practice this means that when the shell in sample B has been grown for 7 minutes it corresponds to a growth-duration of a little over 6 minutes for the shell in sample A. This means that it would be more correct to assume that the shell in sample B was grown for approximately 6 minutes instead of 7 when comparing the characteristics of the two samples.

Al has a lower diffusion length compared to Ga so when the Al content is increased there will be a larger number of atoms unable to climb all the way to the top or all the way to the bottom of the wires. When the length of the wires becomes longer than the Al adatom diffusion length the adatoms will begin to nucleate at the sidewalls of the NWs creating a physical barrier for the Ga adatoms. The Ga adatoms gets trapped at the nucleation sites of the Al adatoms on the sidewalls and combined with the As adatoms this forms a radial growing AlGaAs shell. This also explains why sample B had a lower diameter at the bottom of the wires compared to sample A. Adatoms hitting the sidewalls of the NWs will primarily travel towards the Au-droplet because the chemical potential is lowest there. Tapering towards the bottom of the wires indicates that for some adatoms it would be energetically favourable to migrate down the wires and towards the substrate surface. It is therefore natural that the NWs in sample B are thinner at the bottom than the NWs in sample A. The adatoms that travels towards the substrate surface has a higher probability to get stuck on the way in sample B because of the higher Al content. It is perhaps better to compare the centre-to-bottom diameter ratio from the two samples because the duration of the shell growth differed so much. This ratio was 84/63 ~1.33 for sample B and 81/69 ~1.17 for sample A, in other words sample B had a centre-to-bottom diameter ratio that was around 14% higher than in sample A. Tapering in any direction is not desired, we want the NWs to be as uniform as possible, but unfortunately this appears to be one of the side effects when increasing the radial growth by increasing Al content.

For sample A the average radial-to-axial length ratio was 81/2005 = 0.0404 and for sample B this ratio was 83/1781 = 0.0466, e.g. sample B had approximately a 15% increased radial/axial length ratio compared to sample A. If the shell in sample B had been grown for a longer time the ratio would have increased further because radial growth dominates more and more as the wires become longer than the diffusion length of the adatoms. The difference in radial growth for the different Al content is illustrated in Figure 4.4 with tapering ratio as a function of the diameter at the top of the wires just below the Au-droplet.

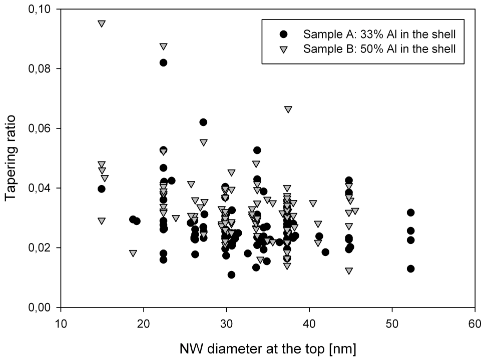

Figure 4.4: Tapering ratio as a function of the diameter at the top of the wires just below the Au-droplet for sample A (black circles) and sample B (gray triangles). Here the tapering ratio is defined as the centre diameter, D_c, subtracted by the diameter at the top, D_t, divided by the wire length at which the tapering started, L_t ($(D_c\text{-}D_t)/L_t$).

If we compare the tapering ratio at different wire top diameters for the two samples we see that sample B has a higher tapering ratio in almost every case and this is another confirmation that a higher Al content results in an increased radial growth.

Figure 4.5 to 4.7 shows NW length as a function of base, centre and top diameter along with histograms for those three regions of the NWs.

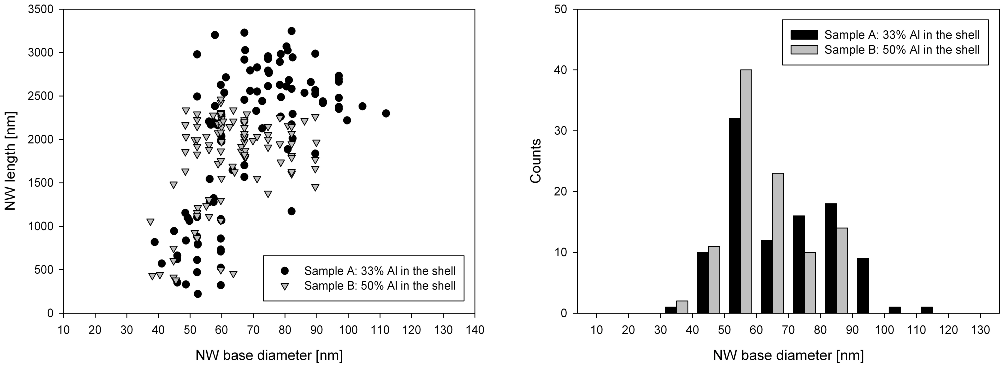

(a) NW length as function of base diameter for sample A(black circles) and sample B(gray triangles). The base diameters were measured at the kinks where the 2D surface layer ended.

(b) Histogram showing the number of NWs within base diameter intervalls of 10 nanometers.

Figure 4.5: Sample B had most wires with base diameter from 30 to 70 nm while sample A had more base diameters from 70 nm up to 120 nm and sample A was the only sample with base diameters larger than 90 nm.

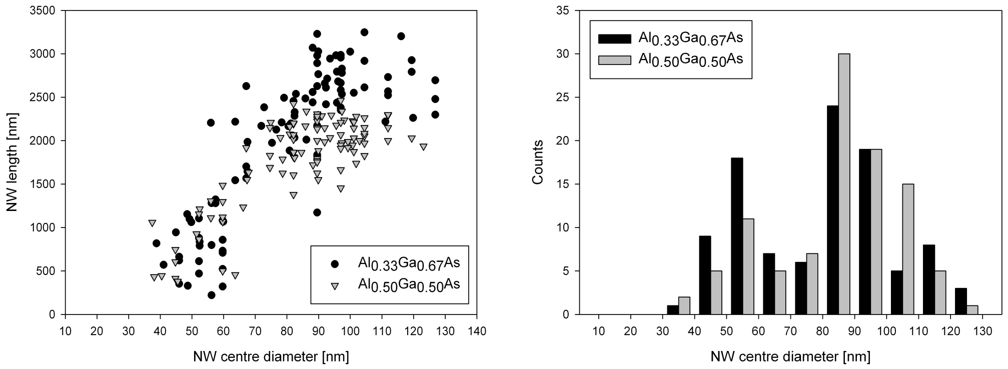

(a) NW length as function of centre diameter for sample A(black circles) and sample B(gray triangles). The diameters were measured at the uniform segments near the centre of the NWs.

(b) Histogram showing the number of NWs within centre diameter intervalls of 10 nanometers.

Figure 4.6: Here sample A, as with the base diameters, also has the highest measured diameter values but sample B has more wires with relatively high diameters, mainly from 80 to 110 nm, with an average of 84 nm.

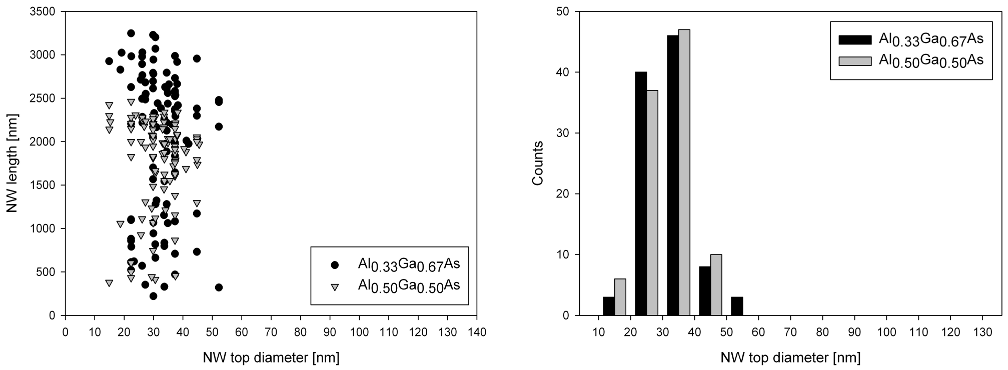

(a) NW length as function of top diameter for sample A(black circles) and sample B(gray triangles). The diameters were measured at the top of the NWs just below the Au droplets.

(b) Histogram showing the number of NWs within top diameter intervalls of 10 nanometers.

Figure 4.7: The top diameter is on an average the same for both samples at 32 nm. This segment is believed to come from purely axial growth and has a much lower Al content than the base of the wires.

As can be seen by Figure 4.5 and 4.6 the length-diameter plots does not coincide well with the 1/d length-diameter dependence from Dubrovskii's growth model [42, 43], see section 2.4 in the Theory chapter. This might be because Dubrovskii's growth model is based on VLS growth and not a mixture of both VLS and VS growth like we have here. The length vs top diameter in Figure 4.7 on the other hand is believed to come mostly from VLS growth and should in theory follow a 1/d dependence. Why this is not the case could mean that the growth model is not entirely accurate for NW diameters around 50 nm and smaller.

From images like those in Figure 4.8, which are birds-eye views of the two samples, the density of NWs were found to be 35 and 39 NWs/μm^2 for sample A and B respectively.

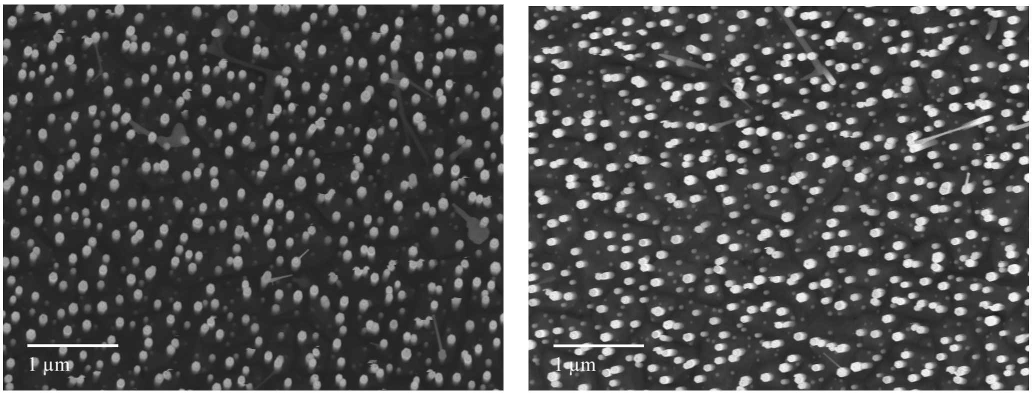

(a) (b)

Figure 4.8: Top view of (a) sample A and (b) sample B to illustrate the density of NWs. The images were obtained with a Zeiss Supra field emission SEM (FE-SEM) operating at 5 kV with a working distance (WD) of 5 mm and a magnification of 15.00K.

4.2 Optical Characterization

To investigate what effect different Al content in the shell had on the optical properties of the GaAs/AlGaAs core-shell NWs the two samples were measured with μ-PL at a temperature of 4.4 K, see section 3.2.3 for details on the PL setup.

Figure 4.9 shows plots of the PL intensity as a function of energy for three different NWs from sample A and corresponding energy Vs. power plots for intensity peaks of interest.

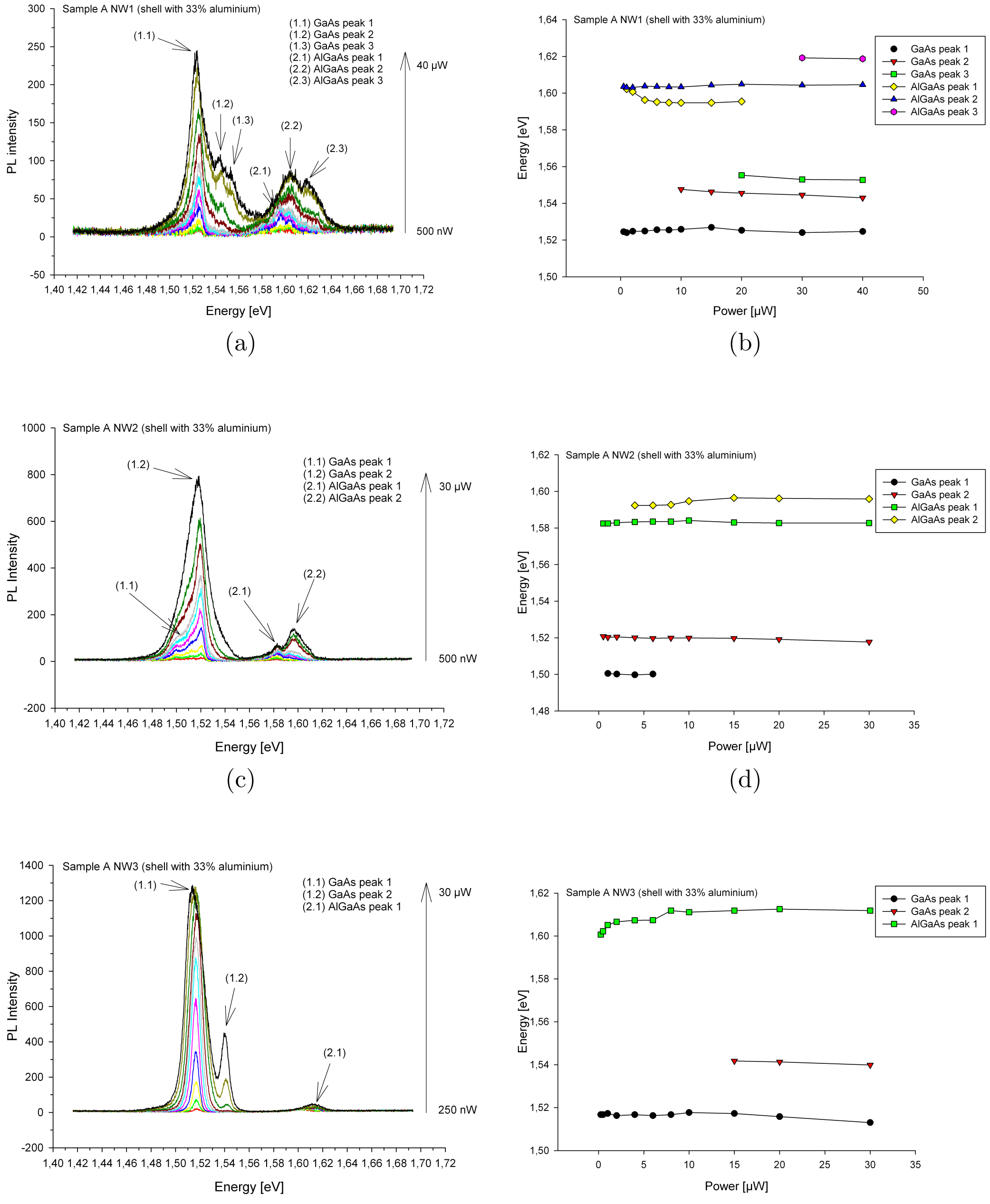

(a) (b)

(c) (d)

(e) (f)

Figure 4.9: Left side: Plot of PL intensity as a function of energy for NW1, NW2 and NW3 from sample A. The power of the incident laser was varied from 250/500 nW to 30/40 μW. The arrows indicate intensity peaks of particular interest. Right side: Plot of energy as a function of power for each of the intensity peaks labelled on the left. The plot shows at what power the peaks start to appear, when they are no longer distinguishable and how they vary in energy with power.

The PL spectra from these three NWs from sample A all show two main emission bands: one related to GaAs emission ranging from ~1.50 to ~1.56 eV, and one related to AlGaAs emission from ~1.58 to ~1.62 eV. If we focus on the emission from the GaAs cores first we see that there are dominating peaks at 1.525, 1.520 and 1.516 eV for NW1, NW2 and NW3 respectively. These energies are close to the free exciton emission energies from bulk ZB GaAs (1.519 at 4.4 K from [30]) Similar results have been found in [29] where single GaAs ZB NWs emitted broad peaks at 1.518±0.003 eV at a temperature of 10 K. This is somewhat misleading because in this study the NWs was confirmed by TEM to have a WZ dominated structure and consequently PL emission from the GaAs cores were expected to lay around 1.544 eV as recently found in *Observation of free exciton photoluminescence emission from single wurtzite GaAs nanowires* by *Hoang et al.* [47]. The NWs grown in this study had a high number of stacking faults leading to short segments of ZB phase within the WZ structure and it's possible that the emissions at ~1,516 - 1,525 eV could originate from these parts of the GaAs cores. This was also suggested in the article by *Hoang et al.* as an explanation for the emission peaks they observed at 1.505 eV in one sample, and 1.515 eV in another of their WZ dominated (but with short ZB segments) GaAs NWs. However the emission peaks corresponding to ZB GaAs were much weaker than the peaks related to WZ GaAs and was only observed in two out of four NW samples in that article. The situation here seems to be almost opposite with weak emission peaks around energies corresponding to GaAs with WZ structure (~1.550 eV in NW1, no peak in NW2 and at ~1.541 eV in NW3) and strong peaks at energies related to emission in GaAs with ZB structure. The reason for this could be that a too low excitation power was used for the PL measurements in this research. It can be seen in Figure 4.9a and 4.9e that the peaks around 1.516 - 1.525 eV are starting to saturate already at an excitation power of 30 μW while the WZ related peaks in the same plots are increasing rapidly. This is especially clear in NW3 from sample A seen in Figure 4.9e where the intensity of the peak at ~1.541 eV increases over eight times more than the intensity of the peak around 1.516 eV when the excitation power is raised from 15 to 30 μW. At higher excitation power we should get a more correct view of the PL spectra where emission peaks around the free exciton energy of WZ GaAs dominate. A similar behaviour is also expected for NW2 from sample A seen in Figure 4.9c: At an excitation power of 30 μW a shoulder is starting to form around 1.54 eV and a peak should begin to appear and even become dominant when the excitation power is increased further.

Another explanation for the emission peaks around 1.516 - 1.525 eV could be defects (carbon) in the GaAs NWs due to contamination of the MBE chamber but these defect peaks should also saturate at higher excitation power.

The PL intensity peaks related to the AlGaAs shell had emission energies from ~1.584 to ~1.620 eV. As discussed in section 2.4.2 growth of the AlGaAs shell also took place in the axial direction on top of the GaAs core and this produced a ~1 μm long AlGaAs section towards the top of the wires. It is most likely that the emission peaks observed at ~1.584 - 1.620 eV stems from those parts of the wires due to their waveguiding properties. The emissions could also come from the AlGaAs shell surrounding the GaAs cores but that is less likely because at this section of the NWs the excitons will have a tendency to diffuse and recombine at the minimum potential in the GaAs core. Along the axial direction there is a substantial difference in the Al content with a high percentage of Al at the bottom of the wires compared to the top. Also there is less Al content in NWs in general compared to 2D film growth as previously argued in section 2.2.1. In sample A the Al content was calibrated to 33% with 2D growth. For a 2D thin film we would then expect an AlGaAs related emission around 1.940 eV at a temperature of 4.4 K using equation 2.7 from section 2.2.1. The emission obtained here from ~1.584 to ~1.620 eV corresponds to an Al content of only 6% to 9% (i.e. 82% to 73% less Al in the NWs compared to the 2D growth calibration). This is quite low but can be explained by the low diffusion length of Al meaning that there is very little Al at the top of the wires where the emissions most likely originate from. In *Growth and photoluminescence characteristics of AlGaAs nanowires* by *Wu et al.* [35] they found that AlGaAs NWs had an Al content of 13% while their reference AlGaAs 2D film had an Al content of 24% (i.e. 46% less Al in the NWs). The higher difference in Al content in the NWs compared to the 2D film, in this study could be because the NWs studied here were atleast twice as long as the NWs studied by *Wu et al.*

The extra peaks/features related to emission from the AlGaAs observed in

NW1 and NW2 could come from variations in the Al composition or from morphological anomalities like defects, twinning, etc. Similar results was found in *Wurtzite GaAs/AlGaAs core-shell nanowires grown by molecular beam epitaxy* by *Hailong et al.* [25] where it was suggested that the AlGaAs part at the top of the NWs could have a self formed core-shell AlGaAs structure with a radial variation in the Al composition (10-15%) and this is a possible explanation for the features raleted to AlGaAs emission observed in this study.

Plots of the PL intensity as a function of energy for three different NWs from sample B and corresponding energy Vs. power plots for intensity peaks of interest are shown in Figure 4.10:

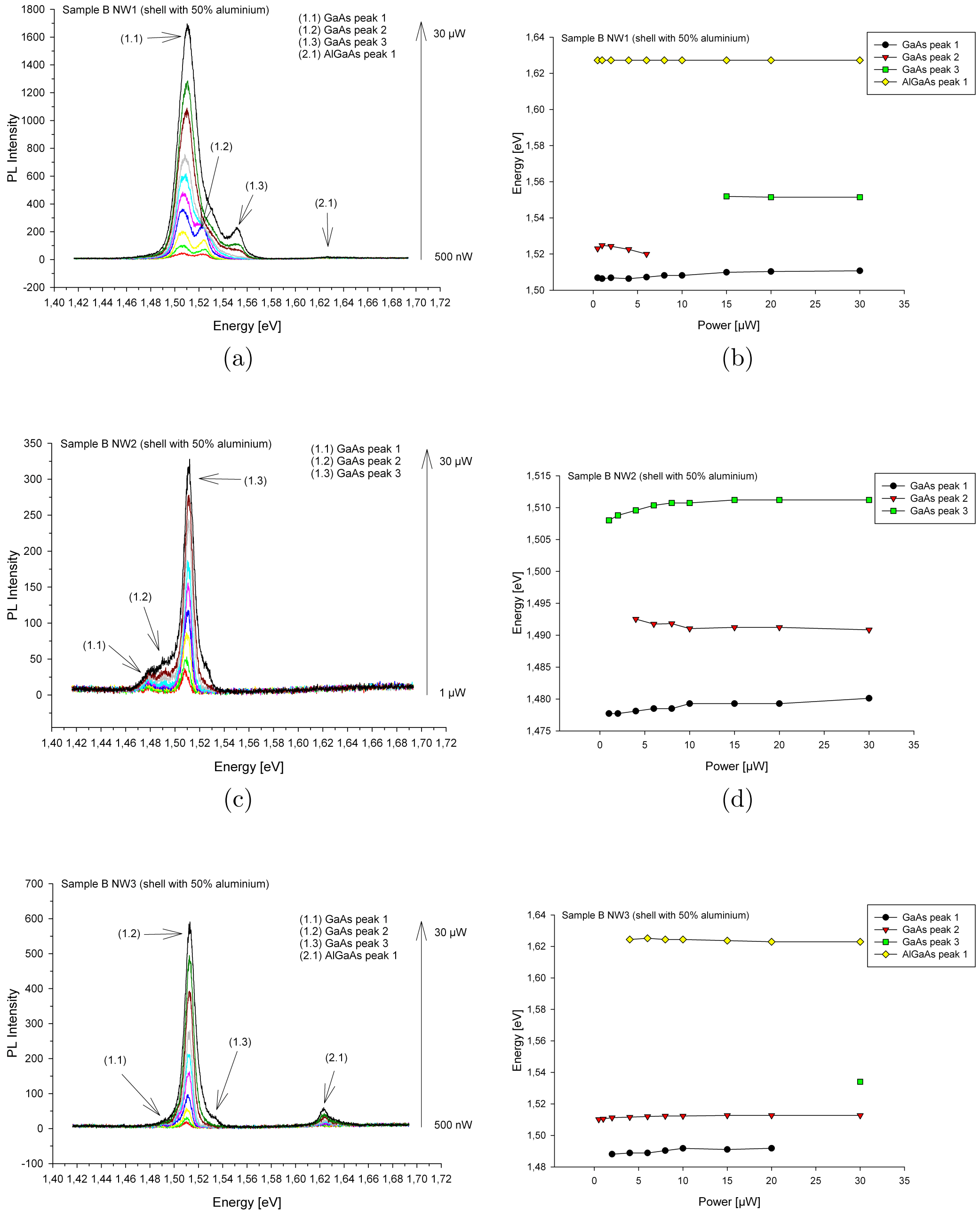

(a) (b)

(c) (d)

(e) (f)

Figure 4.10: Left side: Plot of PL intensity as a function of energy for NW1, NW2 and NW3 from sample B. The power of the incident laser was varied from 0.5/1 μW to 30 μW. The arrows indicate intensity peaks of particular interest. Right side: Plot of energy as a function of power for each of the intensity peaks labelled on the left. The plot shows at what power the peaks start to appear, when they are no longer distinguishable and how they vary in energy with power.

The PL spectra here are overall quite similar to the ones found for the NWs in sample A shown in Figure 4.9 except that the peaks associated with AlGaAs emission in sample B both are at a higher energy (~5 meV - 43 meV) and are quenched compared to the GaAs emission peaks. The move to higher energy for the AlGaAs peaks is simply because sample B had an Al content of 50% compared to 33% for sample A. The reason for the weaker AlGaAs peaks in sample B (almost no peak in NW1, no peak in NW2 and a small peak in NW3) could be because we have a smaller area of pure AlGaAs on top of the GaAs core (due to less VLS growth in the axial direction again because of a higher Al content giving a lower diffusion length) or because the excitons formed in the AlGaAs could have diffused to the GaAs core and then recombined there. A third reason for the weaker AlGaAs peaks in sample B could be that the laser was directed at a slightly different angle for these three NWs compared to the PL measurements in sample A. When conducting the PL measurements the polarisation of the GaAs/AlGaAs core-shell NWs was not considered and the angle at which the laser was directed towards the different NWs was arbitrary. As found in both [48] and [29] this type of core-shell NWs show a strong linear polarization anisotropy emission with the preferential polarization along the nanowire axis. The fact that this was not regarded makes it difficult to compare the optical results from the two samples in their present form and thus these result obtained here are unsufficient to conclude wheter or not an Al content of 50% in the shell is preferential over 33% Al in the shell. TEM measurements of the NWs from both samples could confirm wheter or not the weaker AlGaAs emission comes from shorter AlGaAs segments at the top in sample B but this was not done due to time restrictions.

We also have the same issue here, as in sample A, with strong peaks around 1.51 eV related to emission from ZB segments or defects and weaker peaks/shoulders at ~1.53 - 1.55 eV corresponding to emission from WZ GaAs due to the low excitation power used.

The PL spectra from both samples showed very little shift in energy with power suggesting that quantum confinement effects were not present in any of the wires investigated here. This was expected because the diameter of the GaAs cores examined with PL were all larger than the de Broglie wavelength in GaAs (~20 nm).

For both samples it is clear that the AlGaAs shells improves the PL emission from the GaAs cores. In all the NWs measured by PL there were strong peaks related to GaAs emission. For bare GaAs NWs very small emission peaks have been found when measuring at low temperatures (~4 K) [28], [25] and subsequently a much higher PL emission when the GaAs NWs where coated with AlGaAs shells. This reinforces the belief that AlGaAs acts as a passivation layer supressing non-radiative recombinations at the surface of GaAs.

Chapter 5

Conclusion

In this study GaAs/AlGaAs core-shell NWs with two different Al shell compositions were grown by Au-assisted MBE, one with 33% (sample A) and one with 50% (sample B) Al in the shell. It was found that an increase in Al content in the shell resulted in an increase in radial growth and stronger tapering towards both the top and bottom of the NWs. This is a natural consequence of the shorter diffusion length of Al adatoms compared to Ga adatoms. The NWs were found by TEM measurements to have a WZ structure but with a number of stacking faults producing short segments with ZB phase. Low temperature μ-PL showed strong emission at energies corresponding to GaAs and weak emission at energies corresponding to AlGaAs. Comparison of the PL spectra from the GaAs/AlGaAs core-shell NWs in this study with PL spectra from bare GaAs NWs clearly demonstrates that the AlGaAs shell drastically increases the number of radiative recombinations taking place in the GaAs.

For future work it could be interesting to grow the GaAs cores in a two-temperature procedure as in [49] for the purpose of suppressing stacking faults along the length of the NWs. A number of possible alterations of the growth conditions for the AlGaAs shell should be interesting to conduct like; holding the V/III flux ratio fixed while growing at different temperatures or oppositely holding the temperature fixed while growing at different V/III flux ratios. To better understand the influence different AlGaAs shell thicknesses has on the optical properties of the system a more thorough PL investigation must be conducted, including polarization and temperature dependence together with PL response from high power input.

Bibliography

[1] L. Samuelson, C. Thelander, M. T. Björk, M. Borgström, K. Deppert, K. A. Dick, A. E. Hansen, T. Mårtensson, N. Panev, A. I. Persson, W. Seifert, N. Sköld, M. W. Larsson, and L. R. Wallenberg. Semiconductor nanowires for 0D and 1D physics and applications. *Physica E*, 25(2).

[2] X. Duan, Y. Huang, R. Agarwal, and C. M. Lieber. Single-nanowire electrically driven lasers. *Nature*, 421:241–245, 2003. Available from: `http://www.nature.com/nature/journal/v421/n6920/full/nature01353.html`.

[3] O. Hayden, A. B. Greytak, and D. C. Bell. Core-shell nanowire light-emitting diodes. *Advanced Materials*, 17(6):701 – 704, 2005. Available from: `http://www3.interscience.wiley.com/journal/110429847/abstract?CRETRY=1&SRETRY=0`.

[4] Lincoln J. Lauhon, Mark S. Gudiksen, Deli Wang, and Charles M. Lieber. Epitaxial core–shell and core–multishell nanowire heterostructures. *Nature*, 420:57–61, 2002. Available from: `http://www.nature.com/nature/journal/v420/n6911/full/nature01141.html`.

[5] Li Zhang, Ryan Tu, and Hongjie Dai. Parallel core-shell metal-dielectric-semiconductor Germanium nanowires for high-current surround-gate field-effect transistors. *Nano Lett.*, 6(12):2785–2789, 2006. Available from: `http://pubs.acs.org/doi/abs/10.1021/nl061833b`.

[6] M. Law, L. E. Greene, A. Radenovic, T. Kuykendall, J. Liphardt, and P. D. Yang. ZnO-Al2o3 and ZnO-TiO2 core-shell nanowire dye-sensitized solar cells.

Journal of Physical Chemistry B, 110(45):22652–22663, 2006. Available from: `http://infoscience.epfl.ch/record/129290`.

[7] G. Koley and Zhihua Cai. InN nanowire based sensors. *Sensors, 2008 IEEE*, pages 118 – 121, 2008. Available from: `http://ieeexplore.ieee.org/search/wrapper.jsp?arnumber=4716397`.

[8] Charles Kittel. *Introduction to Solid State Physics*. John Wiley & Sons Inc, eight edition, 2005.

[9] M. T. Björk, B. J. Ohlsson, T. Sass, A. I. Persson, C. Thelander, M. H. Magnusson, K. Deppert, L. R. Wallenberg, and L. Samuelson. One-dimensional steeplechase for electrons realized. *Nano Lett.*, 2(2):87–89, 2002. Available from: `http://pubs.acs.org/doi/abs/10.1021/nl010099n`.

[10] Yiying Wu, Rong Fan, and Peidong Yang. Block-by-block growth of single-crystalline si/sige superlattice nanowires. *Nano Lett.*, 2(2):83–86, 2002. Available from: `http://pubs.acs.org/doi/abs/10.1021/nl0156888`.

[11] Maria Tchernycheva, George E. Cirlin, Gilles Patriarche, Laurent Travers, Valery Zwiller, Umberto Perinetti, and Jean-Christophe Harmand. Growth and characterization of inp nanowires with inasp insertions. *Nano Lett.*, 7(6):1500–1504, 2002. Available from: `http://pubs.acs.org/doi/abs/10.1021/nl070228l`.

[12] Masanari Koguchi, Hiroshi Kakibayashi, Masamitsu Yazawa, Kenji Hiruma, and Toshio Katsuyama. Crystal structure change of gaas and inas whiskers from zinc-blende to wurtzite type. *JJAP*, 31:2061–2065, 1992. Available from: `http://jjap.ipap.jp/link?JJAP/31/2061/`.

[13] Ann I. Persson, Magnus W. Larsson, Stig Stenström, Jonas B. Ohlsson, Lars Samuelson, and Reine L. Wallenberg. Solid-phase diffusion mechanism for gaas nanowire growth. *Nature Materials*, 3:677–681, 2004. Available from: `http://www.nature.com/nmat/journal/v3/n10/abs/nmat1220.html`.

[14] D. L. Dheeraj, G. Patriarche, L. Largeau, H. L. Zhou, A. T. J. van Helvoort, F. Glas, J. C. Harmand, B. O. Fimland, and H. Weman. Zinc

blende gaassb nanowires grown by molecular beam epitaxy. *Nanotechnology*, 19:275605–275608, 2008. Available from: `http://www.iop.org/EJ/abstract/0957-4484/19/27/275605/`.

[15] Jiming Bao, David C. Bell, Federico Capasso, Jakob B. Wagner, Thomas Mårtensson, Johanna Trägårdh, and Lars Samuelson. Optical properties of rotationally twinned InP nanowire heterostructures. *Nano Lett.*, 8(3):836–841, 2008. Available from: `http://pubs.acs.org/doi/abs/10.1021/nl072921e`.

[16] J. Trägårdh, A. I. Persson, J. B. Wagner, D. Hessman, and L. Samuelson. Measurements of the band gap of wurtzite $\mathrm{InAs_{1\text{-}x}P_x}$ nanowires using photocurrent spectroscopy. *JAP*, 101:123701, 2007. Available from: `http://link.aip.org/link/?JAPIAU/101/123701/1`.

[17] Z. Ikonic, G. P. Srivastava, and J. C. Inkson. Electronic structure of twinning superlattices. *Surf. Sci.*, 307.

[18] Z. Ikonic, G. P. Srivastava, and J. C. Inkson. Electronic properties of twin boundaries and twinning superlattices in diamond-type and zinc-blende-type semiconductors. *Phys. Rev. B*, 48:17181–17193, 1993. Available from: `http://prola.aps.org/abstract/PRB/v48/i23/p17181_1`.

[19] W. E. Spicer, P. W. Chye, P. R. Skeath, C. Y. Su, and I. Lindau. New and unified model for Schottky barrier and iii–v insulator interface states formation. *J. Vac. Sci. Technol.*, 16(5):1422–1433, 1979. Available from: `http://dx.doi.org/10.1116/1.570215`.

[20] W. E. Spicer, Z. Lilienthal-Weber, E. Weber, N. Newman, T. Kendelewicz, R. Cao, C. McCants, P. Mahowald, K. Miyano, and I. Lindau. The advanced unified defect model for Schottky barrier formation. *J. Vac. Sci. Technol. B*, 6(4):1245–1251, 1988. Available from: `http://dx.doi.org/10.1116/1.584244`.

[21] V. Heine. Theory of surface states. *Phys. Rev. A*, 138:1689–1696, 1965. Available from: `http://link.aps.org/doi/10.1103/PhysRev.138.A1689`.

[22] J. Tersoff. Schottky barrier heights and the continuum of gap states. *Phys. Rev. Lett.*, 52:465 – 468, 1984. Available from: `http://link.aps.org/doi/10.1103/PhysRevLett.52.465`.

[23] Hideki Hasegawa and Hideo Ohno. Unified disorder induced gap state model for insulator–semiconductor and metal–semiconductor interfaces. *J. Vac. Sci. Technol. B*, 4(4):1130–1138, 1986. Available from: `http://dx.doi.org/10.1116/1.583556`.

[24] J. M. Woodall and J. L. Freeouf. GaAs metallization: Some problems and trends. *J. Vac. Sci. Technol.*, 19(3):794–798, 1981. Available from: `http://dx.doi.org/10.1116/1.571150`.

[25] H. L. Zhou, T. B. Hoang, D. L. Dheeraj, A. T. J. van Helvoort, L. Liu, J. C. Harmand, B. O. Fimland, and H. Weman. Wurtzite GaAs/AlGaAs core-shell nanowires grown by molecular beam epitaxy. *Nanotechnology*, 20:415701–415708, 2009. Available from: `http://www.iop.org/EJ/abstract/0957-4484/20/41/415701/`.

[26] Ki-Ha Hong, Jongseob Kim, Sung-Hoon Lee, and Jai Kwang Shin. Strain-driven electronic band structure modulation of Si nanowires. *Nano Lett.*, 8(5):1335–1340, 2008. Available from: `http://pubs.acs.org/doi/abs/10.1021/nl0734140`.

[27] T. J. Thornton, M. Pepper, H. Ahmed, D. Andrews, and G. J. Davies. One-dimensional conduction in the 2D electron gas of a GaAs-AlGaAs heterojunction. *Phys. Rev. Lett.*, 56(11):1198–1201, 1986. Available from: `http://link.aps.org/doi/10.1103/PhysRevLett.56.1198`.

[28] J. Noborisaka, J. Motohisa, S. Hara, and T. Fukui. Fabrication and characterization of freestanding GaAs/AlGaAs core-shell nanowires and AlGaAs nanotubes by using selective-area metalorganic vapor phase epitaxy. *Appl. Phys. Lett.*, 87:093109, 2005. Available from: `http://link.aip.org/link/?APPLAB/87/093109/1`.

[29] L. V. Titova, Thang B. Hoang, H. E. Jackson, L. M. Smith, J. M. Yarrison-Rice, Y. Kim, H. J. Joyce, H. H. Tan, and C. Jagadish. Temperature dependence of photoluminescence from single core-shell GaAs–AlGaAs nanowires. *Appl. Phys. Lett.*, 89:173126, 2006. Available from: `http://link.aip.org/link/?APPLAB/89/173126/1`.

[30] Ioffe Physical Technical Institute. NSM Archive - Aluminium Gallium Arsenide (AlGaAs) - Band structure and carrier concentration [online]. 2002. Available from: `http://www.ioffe.rssi.ru/SVA/NSM/Semicond/AlGaAs/bandstr.html` [cited 23 October 2002].

[31] Ioffe Physical Technical Institute. Band structure and carrier concentration of Gallium Arsenide (GaAs) [online]. 2009. Available from: `http://www.ioffe.rssi.ru/SVA/NSM/Semicond/GaAs/bandstr.html` [cited 23 October 2002].

[32] Su-Huai Wei and Alex Zunger. InAsSb/InAs: A type-i or a type-ii band alignment. *Phys. Rev. B*, 52(16):12039 – 12044, 1995. Available from: `http://link.aps.org/doi/10.1103/PhysRevB.52.12039`.

[33] Vassil Palankovski. 3.3.1 Bandgap Energy [online]. 2001. Available from: `http://www.iue.tuwien.ac.at/phd/palankovski/node37.html` [cited 23 October 2002].

[34] C. Chen, S. Shehata, C. Fradin, R. LaPierre, C. Couteau, and G. Weihs. Self-directed growth of AlGaAs core-shell nanowires for visible light applications. *Nano Lett.*, 7(9):2584–2589, 2007. Available from: `http://www.ncbi.nlm.nih.gov/pubmed/17696557`.

[35] Z. H. Wu, M. Sun, X. Y. Mei, and H. E. Ruda. Growth and photoluminescence characteristics of algaas nanowires. *App. Phys. Lett.*, 85(4):657, 2004. Available from: `http://link.aip.org/link/?APPLAB/85/657/1`.

[36] G. D. Gilliland. Photoluminescence spectroscopy of crystalline semiconductors. *Materials Science and Engineering*, 18(3).

[37] R. S. Wagner and W. C. Ellis. Vapor-liquid-solid mechanism of single crystal growth. *Appl. Phys. Lett.*, 4(5):89, 1964. Available from: `http://link.aip.org/link/?APPLAB/4/89/1`.

[38] M. Tchernycheva, J.C. Harmand, G. Patriarche, L. Travers, and G.E. Cirlin. Temperature conditions for GaAs nanowire formation by Au-assisted molecular beam epitaxy. *Nanotechnology*, 17:4025–4030, 2006. Available from: `http://www.iop.org/EJ/abstract/0957-4484/17/16/005`.

[39] T. Shitara, J. H. Neave, and B. A. Joyce. Reflection high-energy electron diffraction intensity oscillations and anisotropy on vicinal AlAs(001) during molecular-beam epitaxy. *Appl. Phys. Lett.*, 62(14):1658, 1993. Available from: `http://link.aip.org/link/?APPLAB/62/1658/1`.

[40] T. Shitara, E. Kondo, and T. Nishinaga. RHEED oscillation and surface diffusion length on GaAs(111)B surface. *Journal of Crystal Growth*, 99(1).

[41] Y. Nomura, Y. Morishita, S. Goto, Y. Katayama, and T. Isu. Surface diffusion length of Ga adatoms on $(\bar{1}11)$b surfaces during molecular beam epitaxy. *Appl. Phys. Lett.*, 64:1123, 1994. Available from: `http://link.aip.org/link/?APPLAB/64/1123/1`.

[42] V. G. Dubrovskiia and N. V. Sibirevc. General form of the dependences of nanowire growth rate on the nanowire radius. *Journal of Crystal Growth*, 304(2):504–513, 2007. Available from: `http://dx.doi.org/10.1016/j.jcrysgro.2007.03.034`.

[43] V. G. Dubrovskii, N. V. Sibirev, G. E. Cirlin, J. C. Harmand, and V. M. Ustinov. Theoretical analysis of the vapor-liquid-solid mechanism of nanowire growth during molecular beam epitaxy. *Phys. Rev. E*, 73:021603, 2006. Available from: `http://www.ncbi.nlm.nih.gov/pubmed/16605346`.

[44] K. Barnham and D.D. Vvedensky. *Low-dimensional semiconductor structures; Epitaxial Growth of Semiconductors.* Cambridge University Press, 2001.

[45] Kenji Hiruma, Masamitsu Yazawa, Keiichi Haraguchi, Kensuke Ogawa, Toshio Katsuyama, Masanari Koguchi, and Hiroshi Kakibayashi. GaAs

free-standing quantum-size wires. *JAP*, 74:3162, 1993. Available from: `http://link.aip.org/link/?JAPIAU/74/3162/1`.

[46] D.L. Dheeraj, G. Patriarche, H. Zhou, J.C. Harmand, H. Weman, and B.O. Fimland. Growth and structural characterization of GaAs/GaAsSb axial heterostructured nanowires. *Journal of Crystal Growth*, 311(7):1847–1850, 2009. Available from: `http://dx.doi.org/10.1016/j.jcrysgro.2008.11.090`.

[47] Thang B. Hoang, A. F. Moses, H. L. Zhou, D. L. Dheeraj, B. O. Fimland, and H. Weman. Observation of free exciton photoluminescence emission from single wurtzite GaAs nanowires. *Appl. Phys. Lett.*, 94:133105, 2009. Available from: `http://link.aip.org/link/?APPLAB/94/133105/1`.

[48] Hannah J. Joyce, Y. Kim, Q. Gao, H. H. Tan, and C. Jagadish. Growth, structural and optical properties of GaAs/AlGaAs core/shell nanowires with and without quantum well shells. *Nanoscience and Nanotechnology*, 2006. Available from: `http://ieeexplore.ieee.org/search/wrapper.jsp?arnumber=4143430`.

[49] H.J. Joyce, Y. Kim, Q. Gao, H.H. Tan, and C. Jagadish. Growth, structural and optical properties of GaAs/AlGaAs core/shell nanowires with and without quantum well shells. *Nanoscience and Nanotechnology, ICONN '06. International Conference on 3-7 July 2006.* Available from: `http://ieeexplore.ieee.org/search/wrapper.jsp?arnumber=4143430`.